Published in final edited form as:
Int J Hyperthermia. 2012 ; 28(1): 69–86. doi:10.3109/02656736.2011.630337.

Considerations for theoretical modeling of thermal ablation with catheter-based ultrasonic sources: implications for treatment planning, monitoring and control

Punit Prakash[1,*] and **Chris J. Diederich**[1]

[1]Thermal Therapy Research Group, Department of Radiation Oncology, University of California, San Francisco, 1600 Divisadero Street, Suite H1031 San Francisco, CA 94143 USA. Phone: +1 415 353 9848 Fax: +1 415 353 9883

Abstract

Purpose—To determine the impact of including dynamic changes in tissue physical properties during heating on feedback controlled thermal ablation with catheter-based ultrasound. Additionally, we compared impact several indicators of thermal damage on predicted extents of ablation zones for planning and monitoring ablations with this modality.

Methods—A 3D model of ultrasound ablation with interstitial and transurethral applicators incorporating temperature based feedback control was used to simulate thermal ablations in prostate and liver tissue. We investigated five coupled models of heat dependent changes in tissue acoustic attenuation/absorption and blood perfusion of varying degrees of complexity.. Dimensions of the ablation zone were computed using temperature, thermal dose, and Arrhenius thermal damage indicators of coagulative necrosis. A comparison of the predictions by each of these models was illustrated on a patient-specific anatomy in the treatment planning setting.

Results—Models including dynamic changes in blood perfusion and acoustic attenuation as a function of thermal dose/damage predicted near-identical ablation zone volumes (maximum variation < 2.5%). Accounting for dynamic acoustic attenuation appeared to play a critical role in estimating ablation zone size, as models using constant values for acoustic attenuation predicted ablation zone volumes up to 50% larger or 47% smaller in liver and prostate tissue, respectively. Thermal dose ($t_{43} \geq 240$min) and thermal damage ($\Omega \geq 4.6$) thresholds for coagulative necrosis are in good agreement for all heating durations, temperature thresholds in the range of 54 °C for short (< 5 min) duration ablations and 50 °C for long (15 min) ablations may serve as surrogates for determination of the outer treatment boundary.

Conclusions—Accounting for dynamic changes in acoustic attenuation/absorption appeared to play a critical role in predicted extents of ablation zones. For typical 5—15 min ablations with this modality, thermal dose and Arrhenius damage measures of ablation zone dimensions are in good agreement, while appropriately selected temperature thresholds provide a computationally cheaper surrogate.

Keywords

thermal ablation; high intensity ultrasound; ultrasound ablation; theoretical model; treatment planning

[*]prakashp@radonc.ucsf.edu.

Declaration of Interest

The authors alone are responsible for the contents and writing of the paper.

Introduction

Thermal ablation is increasingly being used for treatment of cancer and benign disease in the liver, kidney, lung, prostate, brain, bone, uterus and other organs [1–3]. High temperature thermal therapy is also widely used for treatment of cardiac arrhythmias and tissue modification and reshaping. In cancer therapy, the goal of thermal ablation therapies is to raise tissue temperature in the target volume to induce coagulative necrosis, while limiting thermal exposure to surrounding tissue. These procedures are usually performed under image guidance to assist in applicator positioning, and when possible, treatment monitoring. Clinically available modalities include cryoablation, lasers, microwaves, radiofrequency (RF) currents, thermal conduction and ultrasound. A major advantage of ultrasound technology over other modalities is enhanced penetration of energy and the ability to control the spatial power deposition pattern, leading to more accurate thermal targeting [4, 5]. High intensity focused ultrasound (HIFU) has the added advantage of being a non-invasive treatment modality, while offering precise control of the heating pattern [5, 6]. However, large target volumes require long treatment times, focusing may be sensitive to respiratory motion, and there is a limited acoustic window for deep-seated targets [7–9]. Minimally invasive catheter-based ultrasound applicators are under development for percutaneous or intraluminal ablation of targets such as the prostate, uterine fibroids, and liver [10–14]. Applicators consisting of linear arrays of independently powered sectored tubular, planar or curvilinear transducers provide spatial control of heating along the length of the applicator and across the angular expanse. *In vivo* studies have demonstrated these devices offer precise, three dimensional (3D) spatial control of heating profiles [4, 12, 14–20]. Compared to currently available RF and microwave technology, catheter-based ultrasound devices currently under development have the potential advantage of affording spatio-temporal control of energy deposition, at the expense of possibly larger catheter diameters [12].

Theoretical models of thermal ablation solve the physical equations governing energy deposition and heat transfer in tissue to determine the transient temperature profile and assess tissue damage upon heating. They are an essential tool during the design and optimization of devices for isolating promising designs for prototyping. Models also form the basis of treatment planning platforms that assist physicians in tailoring thermal therapy procedures to individual patient anatomies [21–25]. Comprehensive modeling of thermal ablation requires knowledge of tissue physical properties that impact energy deposition and heat transfer in tissue. Some of these properties may change substantially during heating, thereby altering the device's power deposition and heating pattern. For ablation with catheter-based (i.e. interstitial and intracavitary) ultrasonic sources, these properties include acoustic attenuation and absorption coefficients, blood perfusion rates, and thermal conductivity [26–29].

Several studies have reported the impact of heating on acoustic absorption and attenuation coefficients of various tissues, in both *in vivo* and *ex vivo* tissue models [30–33]. For soft tissues, acoustic attenuation increases with heating up to a value 2—3 times its nominal value. Thermal conductivity of tissue increases with temperature; at temperatures in excess of 80 °C, thermal conductivity of tissue increases by up to 20% its nominal value at 37 °C [34, 35]. Data from *in vivo* animal models and clinical studies show that microvascular blood perfusion can increase with temperature in the hyperthermic region (41—45 °C) [36–38], before decreasing and subsequent microvascular stasis at higher temperatures. Despite the availability of data showing dynamic changes in tissue properties during heating, many theoretical studies of thermal ablation do not include all of, and some none at all, the relevant changes in tissue properties. Moreover, there have been few studies analyzing the cumulative impact of all relevant parameters for modeling thermal ablation with ultrasonic sources. Many studies use a constant value for tissue acoustic attenuation and absorption

coefficients during ablation [20, 39–44]. For a fixed power and time, models including dynamic changes in attenuation predict smaller ablation zone sizes compared to models excluding increasing attenuation during heating, due to decreased acoustic penetration [26, 28, 45].. Theoretical studies of RF and microwave ablation have shown that the choice of algorithm for dynamic changes in blood perfusion during ablation has a substantial impact on the predicted size of ablation zone [29, 37]. Experimental and simulation studies have shown that changes in tissue absorption during heating results in shifting of the ultrasound field and focal spot during focused ultrasound exposures [46, 47].

Thermal models use the calculated transient temperature profile to estimate extents of thermal necrosis and tissue damage. Models of tissue damage and thermal necrosis, for example, the thermal ioseffective dose model [48] and Arrhenius thermal damage model [49], are a complex function of the time-temperature history during heating. Both of these models have been shown to predict thermal damage accurately *in vivo* [37, 50]. In practice, only limited thermometry information is available during routine ablation treatments. Magnetic resonance imaging (MRI) is increasingly being used for spatial monitoring of the transient temperature profile during ablations. Many studies use the raw temperature data from MR thermometry for determining treatment endpoint [17, 51, 52]. In other studies, the calculated thermal dose/thermal damage is used for feedback control and terminating the treatment [50, 53].

Theoretical models of catheter-based ultrasound ablation have been employed in numerous studies to explore device configurations and assess treatment efficacy. These studies have incorporated several techniques for assessing tissue damage due to thermal exposure and modeling dynamic changes in tissue properties during heating, including: thermal dose thresholds for tissue necrosis, binary changes in blood perfusion based on temperature and thermal dose thresholds, and changes in tissue attenuation based on accrued thermal dose [15, 17, 26, 28, 33, 45, 53–57]. In consideration of the development of 3D patient-specific models for treatment planning and real-time feedback control of treatments, the inclusion of these entire elements increases computational burden, and may not be necessary. As described above, there are dynamic tissue properties to be considered for incorporation into a model, as well as techniques for calculating regions of thermally destroyed tissue.

The objective of this study was to perform a comparative analysis of dynamic changes in tissue physical properties and thermal damage descriptors that we deem essential for comprehensive modeling of feedback control based thermal ablation with catheter-based ultrasonic sources. We implemented a 3D finite element method (FEM) computer model of tissue ablation with catheter-based ultrasound applicators, suitable for treatment of prostate, liver and other soft tissue organs. Temperature-based proportional-integral (PI) controllers were implemented to adjust the power supplied to each active transducer element. In particular, we analyzed the impact of acoustic absorption and attenuation coefficients, and blood perfusion rates on the transient temperature profile during heating. An additional aim of this study was to compare the utility of several models for assessing thermal necrosis upon heating with catheter-based ultrasound devices, and assess their practical feasibility and computational efficiency for treatment planning, monitoring and determination of treatment endpoint. Finally, we illustrated the feasibility of employing these models and algorithms for patient-specific planning of thermal ablation therapies.

Methods

Catheter-based ultrasound applicators for thermal ablation

Catheter-based ultrasound devices with tubular transducer arrays are being developed for thermal ablation, and consist of linear arrays of independently powered, ultrasound

transducers. Control of power deposition along the length of the applicator is achieved by tailoring power supplied to each individual transducer. These transducers may be modified to create individually powered sectors providing control of the power deposition in angle. Cooling water is circulated within the applicator to enhance power output and thermal penetration. In this study, we considered two types of applicators – smaller diameter applicators suitable for interstitial or percutaneous insertion directly into the tumor volume [13, 55], and larger diameter applicators suitable for transurethral targeting of prostate [15, 54], each using sectored and unsectored tubular transducers. We restricted this study to simulating thermal ablation with catheter-based ultrasound applicators in prostate and liver targets, as these two tissue types and target definitions bracket the intended field of use of these devices and subsequent treatment modeling and planning strategies.

Interstitial applicators consist of tubular transducers, 1.5 mm outer diameter (OD), operated at a frequency in the range 6.5—8 MHz. The transducer array is enclosed in a 2.4 mm (OD) catheter with water cooling to protect the transducers during sonication. These applicators are under development and have shown potential for treatment of soft tissue targets such as the prostate, liver, brain, kidney, and uterine fibroids. Thermal ablation in the prostate for treatment of cancer or benign disease requires precise localization of heating due to the potential of heating critical structures such as the neurovascular bundles, rectum, and bladder. Sectored applicators may be used individually to ablate a quadrant of the prostate, suitable for treatment of localized prostate cancer; alternatively, multiple unsectored and/or sectored applicators may be used simultaneously for thermal ablation of the entire gland. Therefore, we considered 90°, 180° and 360° applicators for ablation in prostatic targets. Physicians treating liver tumors, which are generally spherical in shape, aim to create large spherical ablation zones that completely encompass the tumor and a safety margin. Thus, we only considered 360° applicators for treating targets in the liver. All interstitial applicators consisted of two 10 mm long transducers, spaced 2 mm apart.

The transurethral applicator is comprised of two 3.5 mm (OD) transducers, 10 mm long, spaced 2 mm apart, and operated at a frequency in the range 6.5—8 MHz, suitable for transurethral prostate therapy. The transducers are enclosed in a water-filled balloon for distention and cooling of the urethra interface. A distal balloon is used to secure the device at the bladder neck. Transurethral applicators are typically sectored to ablate a 90° portion of the prostate. Single sector devices may be employed for treatment of prostate cancer, while dual-sectored devices may be used for treatment of benign prostatic hyperplasia (BPH). The design schema of interstitial and transurethral devices as modeled in this study, are shown in Figure 1.

Coupled acoustic-thermal model for ultrasonic ablation

We developed a 3D coupled acoustic-thermal model using the finite element method (FEM) to determine the transient temperature profile in tissue, when heated with interstitial and transurethral ultrasound applicators. Heat transfer in tissue was modeled with the Pennes bioheat equation [58]:

$$\rho c\frac{\partial T}{\partial t}=\nabla\cdot k\nabla T+Q_s-\dot{m}_{bl}c_{bl}(T-T_{bl}) \quad (1)$$

where ρ [kg m^{-3}] is tissue density, c [J kg^{-1} K^{-1}]is tissue specific heat capacity, T[K] is temperature, k [W m^{-1} K^{-1}] is tissue thermal conductivity, Q_s [W m^{-3}] is acoustic power deposited, $\dot{m}_{bl}$ [kg m^{-3} s^{-1}] is blood mass perfusion rate, c_{bl} [J kg^{-1} K^{-1}] is specific heat capacity of blood and T_{bl} [K] is temperature of inflowing arterial blood. Table I lists nominal values for tissue properties considered in this study. For tubular ultrasound sources,

the acoustic power deposition emitted along the length of each transducer segment is given by (Equation 2):

$$Q_s = 2\alpha I_s \frac{r_0}{r} \exp\left(-2\int \mu r' dr'\right) \quad (2)$$

where α is acoustic absorption coefficient, I_s is intensity on the transducer surface, r_0 is radius of the transducer, r is radial distance from the transducer center, μ is acoustic attenuation coefficient, and r' is radial distance from the transducer surface [59]. The cumulative heat source is obtained by summing up the contribution of all transducers. Maximum power supplied to each transducer segment was set to 15 W and 20 W for interstitial and transurethral applicators, respectively. Independent PI controllers were employed to modulate power supplied to each transducer/transducer sector in order to limit peak tissue temperatures to 90 °C. The same controller coefficients (k_p = 0.5, k_i = 0.004) were used for all feedback-control simulations. Maximal temperatures in the plane through the center of each transducer sector were sampled every 10 s and used to update applied electrical power. The sampling time of 10 s was selected to investigate modeling and control parameters based upon update intervals typical for currently available multi-slice MR thermometry for monitoring and controlling thermal ablation procedures [60]. In order to gain an appreciation for the impact of feedback control on any differences observed between models, open-loop ablations (no feedback control) were also simulated for 180° interstitial applicators in prostate tissue. A constant 10 W was applied to each transducer segment for 15 mins. This power level was selected as it was the highest power level to yield tissue temperatures below 100 °C (above which tissue water vaporisation and subsequent unpredictable heating may occur due to the presence of bubbles).

The FEM model was implemented in COMSOL Multiphysics v3.5a (COMSOL Inc., Burlington, MA) and all post-processing was performed with MATLAB (The Mathworks, Inc., Natick, MA). Initial tissue temperature ($T_0 = T_{bl}$) was set to 37 °C. Boundary conditions on the edges of the modeled tissue (10 cm × 10 cm × 8 cm) were set to a fixed temperature of 37 °C. A convective heat transfer boundary condition (equation 3), with h = 500 W m^{-1} K^{-1} and T_∞ = 25 °C, was applied at the inner catheter wall.

$$\vec{n} \cdot k\nabla T = h(T_\infty - T) \quad (3)$$

Quadratic Lagrangian elements were used to discretize the solution space. A sub-millimeter mesh resolution (maximum element edge length ~ 0.5 mm) was employed at the surface of the applicators, with progressively increasing mesh element size away from the applicator, with maximum element edge length restricted to 3 mm within the entire computational domain. A nonlinear, implicit solver with variable time steps ($0.001 < \Delta t < 5$ s) was used to solve the transient bioheat equation for 15 min ablations. A Cauchy convergence test was performed to ensure that the selected mesh resolution did not impact the quality of the solution. Thermal dose and Arrhenius tissue damage calculations were updated at each time step and used to update values of tissue physical properties, as described in the following sections.

Asssessment of tissue damage due to heat

Thermal damage is a complex function of the time-temperature history during heating. Several models of thermal injury and destruction due to heating have been reported in the literature and have been reviewed in Dewhirst *et al.* [61] and Dewey [62]. Henriques [49] modeled cell-death as a two-state, first-order kinetics process using the Arrhenius equation. This technique has been used to predict thermal tissue damage and physical changes associated with thermal exposure in several tissue types [25, 63–69]. Equation 5 describes

the rate process, while Equation 6 describes how the value Ω is related to the ratio of damaged to undamaged cells after heating for duration *t*.

$$\Omega(t)=\int_0^t A\exp[-\Delta E/RT(t)]d\tau \tag{5}$$

$$\Omega(t)=-\ln\frac{c(t)}{c(t_0)} \tag{6}$$

The parameters ΔE, activation energy, and A, frequency factor, are specific to tissue type, and need to be established experimentally. He *et al.* [66] have reviewed techniques for measuring the Arrhenius parameters, ΔE and A, using different indicators for assessing thermal damage in prostate and kidney tissue. Borrelli *et al.* [70] measured rate process parameters for baby hamster kidney cells heated up to 57 °C. Parameters for ΔE and A reported in [66] and [70] have been used in several simulation studies to compute thermal damage after ablation of prostate targets. Similar to other simulation studies of liver ablation [29], we employed Arrhenius parameters reported in [70] for estimating thermal damage in liver tissue. Parameter values for ΔE and A used in this study are listed in Table I.

Sapareto and Dewey [48] presented a thermal isoeffective dose model where non-isothermal heating can be compared to isothermal heating at a reference temperature, which is typically 43 °C. The cumulative equivalent thermal dose of heating at 43 °C is given by equation (4).

$$t_{43}=\int_0^t R^{(43^\circ C-T(\tau))}d\tau,\begin{cases} R=0.25, T<43\,^\circ C \\ R=0.5, T\geq 43\,^\circ C \end{cases} \tag{4}$$

For most soft tissues, the threshold for coagulative necrosis is within the range $100 < t_{43} < 1000$ min [61, 62]. A threshold of $t_{43} \geq 240$ min has been shown to correspond to coagulative necrosis and is therefore used as an indicator of treatment endpoint for most soft tissues [62, 68, 71, 72]. The thermal isoeffective dose model is derived from the Arrhenius equation, and more details of the derivation can be found clearly outlined in [61, 62, 69, 73].

Some computational and *in vivo* studies of thermal ablation have used temperature isotherms for assessment of extent of the ablation zone, as well as a control feedback parameter for indicating adequate ablation [20]. Temperature is readily measured during ablations through invasive thermometry or, more recently, with magnetic resonance thermometry. Temperature thresholds in the range 50—60 °C have been used as indicators of treatment endpoint using various thermal ablation modalities; These temperature thresholds are dependent on the attained temperature and treatment duration and have been demonstrated to be within 50–55 °C for catheter-based ultrasound[20, 74, 75]. In this study, we compared thermal dose and thermal damage indicators of necrosis to temperature thresholds in the range 50—54 °C for the 5—15 min ablations.

At each time step, thermal dose and thermal damage were calculated by numerical integration of the transient temperature profile. These data were used to determine appropriate changes in tissue properties depending on the tissue model being employed. Upon termination of heating, these damage measures were used to estimate volume and radial penetration of the ablation zones and extents to which thermal toxicity occurs.

Tissue models

We considered thermal ablation with interstitial and transurethral ultrasound applicators in representative numerical models of prostate and liver tissue. Table I lists nominal values of

tissue acoustic and thermal properties for both prostate and liver tissue. In addition, we incorporated into our models dynamic changes in acoustic attenuation/absorption coefficients, microvascular blood perfusion and thermal conductivity.

Damianou *et al.* [31] measured ultrasonic attenuation and absorption coefficients during heating, as a function of thermal isoeffective dose (t_{43}) and temperature. They noted acoustic attenuation/absorption increases linearly with the logarithm of thermal dose and temperature, until it attains a value approximately double its value at basal temperature (Figure 2a). Above an upper threshold, acoustic attenuation/absorption ceased to increase with further heating. Similar results were reported by Clarke *et al.* [30], Worthington *et al.* [32], and Tyreus and Diederich [33].

With moderate heating, blood flow can increase as the body attempts to carry excess heat away in order to maintain basal temperature [36, 76, 77]. With further heating, however, the rate of blood flow diminishes, before subsequent vascular stasis at elevated temperatures. Models of perfusion varying as functions of temperature and thermal dose have been used for simulating thermal ablation and hyperthermia [55, 77]. He *et al.* [37] used a nonlinear data fitting technique to determine a blood perfusion profile in porcine kidney, that resulted in the best match between theoretically computed temperature profiles and temperature measurements during *in vivo* ablations using a microwave applicator. They used an Arrhenius model (Equation 5) to estimate the degree of vascular stasis (DS) based on the transient temperature profile during heating, and varied blood perfusion as a function of DS.

In this study, we considered five different models to describe changes in tissue properties during ablation (Table II). In all models, tissue specific heat capacity and density were held constant, while thermal conductivity increased linearly with temperature. The differences between the models were the manner in which changes in acoustic attenuation/absorption coefficient and blood perfusion rates were modified during ablation. Models 1—3 adjust the acoustic absorption/attenuation coefficients as a function of the logarithm of accumulated thermal dose (t_{43}). This relationship is illustrated in Figure 2a. In model 1, blood perfusion was adjusted using a piecewise linear representation of He *et al.*'s [37] model, proposed by Schutt and Haemmerich [29] and illustrated in Figure 2b. This model calculates the degree of vascular stasis using an Arrhenius relationship (equation 3), with coefficients $A = 1.98 \times 10^{106}\ s^{-1}$ and $\Delta E_a = 6.67 \times 10^5\ J\ mol^{-1}$. Note that these coefficients are specific to blood perfusion changes, and are unrelated to the coefficients for tissue thermal damage described earlier. Blood perfusion in model 2 is adjusted using a similar relationship to model 1, however, the thresholds are determined based on t_{43}. Model 3 adjusts blood perfusion as a step function of thermal dose (t_{43}) – a nominal value for blood perfusion is used while $t_{43} <$ 300 min. Above a threshold dose of $t_{43} \geq 300$ min, blood perfusion is set to zero. Model 4, adjusts acoustic attenuation/absorption coefficient as a function of temperature. The attenuation/absorption coefficient increases linearly with temperature in the range $50 \leq T \leq 65$ °C, as reported by Damianou *et al.* [31]. Blood perfusion is adjusted in a manner similar to models 1 and 2, however, using temperature thresholds. Lastly, the most simplistic model (model 5), uses a constant value for tissue attenuation/absorption, while modeling blood perfusion as a step function of temperature. Each of these models was implemented using nominal values for representative prostate and liver tissue, as listed in Table I. Formulas and thresholds for variations in acoustic attenuation/absorption coefficient and blood perfusion rates are presented in Table II. In all models, we employed a temperature coefficient of 0.2 %/°C for tissue thermal conductivity [35].

Patient-specific planning of thermal ablation

Selected models from above were also implemented in a 3D patient specific treatment planning platform currently under development for thermal ablation with the catheter-based

ultrasound technology. To illustrate the implementation of patient-specific treatment plans with these models,, forward treatment plans for two types of ultrasound ablation treatments in prostate were calculated. Sequential computed tomography (CT) slices of patients with representative anatomies were contoured manually using the Oncentra MasterPlan (Nucletron B.V., Veenendaal, The Netherlands) radiotherapy treatment planning tools to delineate the target, prostate, rectum and bladder. These contours were then imported into the FEM modeling environment, where the 3D patient anatomy was reconstructed. The transient temperature distributions were solved with ultrasound applicators positioned for two treatment strategies: (1) sectored transurethral applicator and (2) sectored interstitial applicator to ablate localized prostate cancer in the posterior quadrant of the prostate gland. In each case, dynamic changes in tissue properties were included using tissue model 3. Independent PI controllers for each transducer segment were employed to limit peak tissue temperatures to 90 °C. Treatment monitoring points ("pilot points") along the outer boundary of the target were identified and associated with each active transducer. Power supplied to each transducer was allowed to reach 12 W and 15 W maximum for interstitial and transurethral applicators, respectively and reduced to 0 W after thermal dose at corresponding pilot points exceeded a threshold of $t_{43} \geq 240$ min. In order to account for accrued thermal dose, treatment simulations were continued for 2 min after power to all transducer sectors was set to 0 W.

Results

Models of dynamic changes in tissue properties

To study the impact of using different models for dynamic changes in tissue properties during ablation, we modeled 5—15 min ablations in prostate and liver targets using interstitial and transurethral applicators. Interstitial applicators with 90°, 180°, or 360° sonication patterns and transurethral applicators with 90° sectored transducers were modeled. Extents of the ablation zone, as measured by critical temperature, thermal dose and thermal damage thresholds were calculated at the end of each time step and at completion of the treatment. Table III lists volumes of the ablation zone as determined by different measures for each of the tissue models 1—5, after 5, 10 and 15 min ablations. Figure 7 summarizes the radial depth of the ablation zone after 15 min treatments for interstitial applicators in prostate and liver tissue when using tissue models 1—5. Figure 4a shows the radial depth of the ablation zone after 15 min ablations for transurethral applicators in prostate and liver tissue when using tissue models 1— 5. Simulations were performed using three different blood perfusion rates, to illustrate the impact of varying blood perfusion levels.

Near identical values for radial depth and volume of ablation zones are obtained using models 1—3 when modeling ablations in prostate tissue with interstitial and transurethral applicators. At a nominal perfusion rate of 2.5 kg m^{-3} s^{-1}, ablation zone volumes for 5—15 min ablations computed using models 2 and 3 are all within 2.6% of those computed using model 1. For ablation in liver tissue using interstitial applicators, models 2 and 3 predict ablation zone volumes within 4.2% and 8.7%, respectively, of those predicted by model 1. Even though model 3 employs a binary change in blood perfusion above a threshold thermal dose, the volume/radial depth of the ablation zone after 15 min heating is nearly identical to models 1 and 2. Model 4, which uses a temperature-based model for adjusting acoustic attenuation coefficients and blood perfusion rates, estimates smaller values for volume and radial depth of the ablation zone, compared to models 1—3. In prostate tissue, ablation zone volumes computed using model 4 are 5.3—14.7% smaller than those computed with model 1. In liver tissue, the ablation zone volumes computed by model 4 are 11.1 (5 min)—26.8% (15 min) smaller than those computed by model 1.

In addition to assessing the extents of the ablation zone (zone of coagulative necrosis), theoretical models are useful to determine the safety of an ablation procedure. That is, models may be used to determine the extent to which thermal toxicity occurs, to in order to evaluate the risk of potential damage to adjacent critical structures. The T = 43 °C isotherm is a metric of the onset of thermal toxicity that has been used in the literature for assessing thermal safety [78]. Fig. 5 shows the radial extent of the onset of thermal toxicity after 5—15 min ablations with a 180° interstitial applicator in a prostate target computed using tissue models 1—5. Radial depth of the T = 43 °C contours computed using models 1—4 are within 3.3% of each other for 5 min ablations, and 6.0% of each other for 15 min ablations. Radial depth of the T = 43 °C contours after 5—15 min ablations computed using model 5 are 22.8%—25.1% larger than those computed using model 1.

The models implemented in this study included a feedback control algorithm that adjusted power levels so as to maintain maximum tissue temperatures associated with each active element at T_{set} = 90 °C. The choice of tissue model used to simulate the ablation affects the computed maximal tissue temperatures, and therefore the applied power levels. To study the impact of the choice of tissue model on the control algorithm, we simulated 15 min ablations with 180° interstitial applicators in a prostate target. Fig. 6a shows the time taken to reach T_{set} = 90 °C when using tissue models 1—5 to model ablations both with and without feedback control. The time taken to reach a temperature of 90 °C are within 3.4% using models 1—3 regardless of whether or not a controller is used. Using model 4, time taken to 90 °C is 12.5%—16.1% larger than when using model 1. Using model 5, time taken to 90 °C is 45.2% larger than when using model 1 if a controller is employed. Without a controller, a temperature of 90 °C is not attained in 15 min of heating when using tissue model 5. Fig. 6b shows the transient evolution of power applied to a 180° ultrasound sector during a 15 min ablation using the feedback controller, when simulated using tissue models 1—5. While power trajectories computed using models 1—4 are quite similar, a substantially different power trajectory (greater power levels for longer durations of time) is computed using model 5.

Metrics for assessing thermal damage

For each of the applicator/tissue configurations explored in this study, we calculated radial depth and volume of the ablation zone as measured by critical thresholds of temperature (50, 52, and 54°C), thermal dose (240 min) and thermal damage ($\Omega \geq 4.6$) metrics. Figure 4 summarizes the radial depth of the ablation zone during the course of 15 min ablations with interstitial applicators in prostate and liver tissue. Figure 4b. shows the radial depth of the ablation zone during the course of a 15 min ablation in prostate tissue with a transurethral applicator. Figures 4b and 7 display data collected using tissue model 1, the most comprehensive model of dynamic changes in tissue properties during heating.

Patient-specific treatment plans

In order to investigate the utility of these theoretical models for treatment planning, we created patient-specific treatment plans for prostate ablations using interstitial and transurethral devices. Figure 8 shows the final temperature profiles and regions of thermal destruction calculated for an interstitial 90° sectored applicator positioned in the posterior portion of a prostate, directing energy toward a focal region of prostate cancer in the peripheral region. Similarly, Figure 9 shows temperature and dose metrics for the case of a 90° sectored transurethral applicator aiming from the urethra towards the target in the posterior portion of the prostate. For each of these cases, the critical temperature (T ≥ 52 °C), thermal dose ($t_{43} \geq 240$ min) and thermal damage ($\Omega \geq 4.6$) clouds are shown to be in close agreement. PI control to regulate maximum temperature, as well as pilot-point control

on the target boundary was used for each of these cases, with applied power durations of 530 s (case 1) and 490 s (case 2).

Discussion

This study was initiated to explore various models for dynamic tissue changes and to determine the best approaches for comprehensive modeling of the temperature distributions and for calculation of thermal tissue destruction during catheter-based ultrasound ablation incorporating temperature based feedback control. We considered five models for dynamic changes in tissue properties. Models 1—3 are based on *in vivo* measurements of tissue properties during and after heating, whereas models 4 and 5 are simplified models often used in simulation studies (Table II). As shown in Figures 3 and 4a, and Table III, near identical values for radial depth and volume of ablation zones are obtained using models 1—3 for 5—15 min ablations. These models all adjust acoustic attenuation/absorption using the same method (linear with the logarithm of accrued thermal dose), while adjusting blood perfusions using varying thresholds of thermal damage or thermal dose. This can be attributed to the steepness of thermal dose/thermal damage gradients near the edge of the ablation zone. As a result, even small changes in temperature result in large changes in thermal dose (see Figure 10). Thus, the effective changes in perfusion between models 1—3 are likely quite similar to each other. Model 4, which adjusts acoustic attenuation/absorption and blood perfusion based on temperature thresholds, estimates smaller values for volume and radial depth of the ablation zone, compared to models 1—3. As shown in Table III, differences in ablation zone volumes computed using model 4 compared to model 1, are smaller for short duration ablations (5 min) compared to longer (10—15 min) ablations. Additionally, differences between ablation zone volumes computed using model 4 and model 1 are larger for ablations in liver tissue (11.1—26.8%) compared to prostate (5.3—14.6%). For longer duration ablations (> 5 min), temperature at radial distances 10 – 15 mm away from the applicator may be in 48—50 °C range, even though accumulated thermal dose may be quite high. Thus, the tissue models tested herein with temperature mediated perfusion models (models 4 and 5) will tend to maintain nominal perfusion values longer than the thermal dose/damage-based perfusion functions (models 1—3), which can result in smaller size of the predicted ablation zone. It is noted that model 4 also includes a temperature-based model for attenuation changes and that the perfusion model may not be solely responsible for the observed differences.. Models employing only temperature dependent changes in tissue properties are less comprehensive representations than those taking into account the time-temperature history. Nevertheless, they require fewer computational resources and include some consideration of changes in tissue dynamics, which are completely neglected in homogeneous tissue models.

As the tissue absorption coefficient increases during heating, the rise in temperature due to incident acoustic energy increases proportionally, whereas with a constant attenuation model (model 5) the rise does not change. This also has the effect of less energy propagating further out into tissue. Thus, when using a constant value for the tissue absorption/attenuation coefficient (model 5), tissue in regions further away from the applicator receive more energy than in models that consider changes in absorption/attenuation coefficients (models 1—4). This results in values for extents of the ablation zone and thermal toxicity, as shown in Figures 3—5. For the same reason, models that do not account for increases in absorption coefficient (model 5) compute lower values for tissue maximum temperatures (Figure 6). The feedback control algorithm considered in this study modulates applied power based on maximal tissue temperature associated with each transducer. Since maximal tissue temperatures computed using model 5 are lower than those computed using models 1—4, the power calculated by the feedback control algorithm when using model 5 will be greater, as seen in Figure 6.

We modeled several applicator designs – interstitial (sectored and unsectored) and transurethral (sectored) – under development for ablation of targets in the prostate, to determine the relative importance of tissue models for all the applicator designs. In addition to computing predicted radial depth of ablation zones, we computed volumes of the ablation zone to account for any differences in extents of the ablation zone near the edges of transducer sector cuts. For all applicators in prostate tissue, extents of the ablation zone computed using model 5 were substantially greater than those computed using model 5. The difference between models 1—4 and model 5 were greater for 90° applicators compared to 180° and 360° applicators. This is explained by the fact that the applied electrical power to each active transducer segment was consistent across all test cases, and thus the acoustic power deposited for 90° applicators was proportionally larger compared to the 180° and 360° devices at the onset of heating.

In liver tissue, however, where the blood perfusion rate is higher (15 kg m^{-3} s^{-1}) and acoustic absorption coefficient (4.5 Np m^{-1} MHz^{-1}) is lower, model 5 estimates smaller radial depths and volumes of ablation zones than the other models (47.1% smaller than model 1). Compared to prostate tissue, a much larger amount of energy is required to overcome the perfusion heat sink and induce thermal necrosis. As tissue heats up, acoustic absorption increases, thereby increasing the rate of local tissue heating. Due to the larger absorption coefficient, the large perfusion heat sink can be overcome to yield therapeutic temperatures. Models that do not account for increased ultrasound absorption during heating will not properly account for the absorbed power in tissue and resultant heat source. In highly perfused tissue such as liver, this may lead to reduced ablation zone predictions.

These results indicate the stark differences in indicators of treatment zone, safety, and implications for controller design, when modeling thermal ablation of tissue catheter-based ultrasound applicators using tissue models of varying complexity. The role of acoustic attenuation/absorption and blood perfusion are particularly important. For treatment planning and monitoring purposes, the exact model used to vary the tissue properties (temperature, thermal dose or thermal damage) are not as important as including some appreciation for the changes in these properties during heating. These results are in agreement with other reports, which show that size of the ablation zone created by focused planar transducers is overestimated when using tissue models that do not include dynamic changes in tissue absorption/attenuation during heating [26, 28, 45, 57]. Schutt and Haemmerich [29] studied the impact of microvascular blood perfusion models on the sizes of ablation zones created during RF ablation in liver tissue. Their results show that models which assume a fixed perfusion rate below a threshold temperature of 60 °C, and zero perfusion above this threshold, estimate smaller sizes of ablation zone compared to models that adjust the blood perfusion rate as a function of tissue damage. Similarly, our simulations in liver tissue (Figure 3D) using a similar perfusion model (model 5) predicted reduced ablation zone sizes, although we note that this model also incorporated a constant tissue attenuation coefficient.

The transient growth of the ablation zone as measured by temperature, thermal dose and thermal damage metrics are shown in Figures 4b and 7. Typical thresholds for each of the measures of extents of the ablation zone (as indicated by thermal necrosis) are shown. Using temperature thresholds for these specific catheter-based ultrasound applicators, it is important to consider the duration of the treatment. For short duration treatments, a temperature threshold of $T \geq 54$ °C is in close agreement with thermal dose and thermal damage measures of the extent of necrosis. However, at longer treatment durations, lower thresholds closer to $T \geq 50$ °C are more suitable. The Arrhenius damage indicator, with appropriate parameters chosen for the specific tissue type, is one appropriate method to model thermal damage due to heating. However, as indicated in the literature, it may be

difficult to obtain parameters for every tissue type, as may be required for patient-specific treatment planning [66]. Recent studies have demonstrated that even small changes in Arrhenius model parameters may have a large impact on estimates of thermal damage [73], although, in contrast, other studies have shown good correlation between experimentally measured damage and predictions using general Arrhenius coefficients [75]. Thermal dose is another measure which takes into account the time-temperature history, and requires a single set of R values and is another suitable model for thermal damage of most tissue types when heated to moderate—high temperatures up to approximately 60 °C [68, 70, 79, 80]. It is noted that there are some studies that suggest the thermal isoeffective dose model is not accurate above ~50 °C [66, 73]. A critical thermal dose threshold indicating a desired level of thermal damage can be established for each tissue type. *In vivo* studies with interstitial and transurethral ultrasound devices have shown good agreement between t_{43} = 120—240 min and thermal damage zones at the outer boundary of lesions generated in brain and prostate [74, 81–83]. The results presented here indicate that, for 5—15 min ablations typical with this energy modality, a critical thermal dose of $t_{43} \geq 240$ min agrees well with other thermal damage measures presented in the literature. Figure 10 illustrates temperature, thermal dose and thermal damage profiles in the radial direction from a 180° interstitial applicator after a 15 min ablation. It is evident from these contours that the temperature, thermal dose and thermal damage gradients are extremely steep at the edges of the ablation zone, and that even large changes in t_{43} (100—1000 min) and Ω (4.6—0.5) yield changes in radial depth of the ablation zone of 1.0 mm and 1.9 mm, respectively. This level of precision in estimating extents of the ablation zone is suitable for treatment planning and monitoring purposes, given the uncertainties in knowledge of patient-specific tissue properties.

The results presented in this study are in good agreement with other quantitative analyses of thermal dose and thermal injury measures. Yung *et al.* [75] reported that critical thermal dose ($t_{43} \geq 240$ min), thermal damage ($\Omega \geq 1$), and temperature ($T \geq 57$ °C) thresholds predict extents of the ablation zone in close agreement with contrast-enhanced MRI immediately following short duration (1—4 min) *in vivo* laser ablation of canine brain. Due to the steep gradients of the thermal damage and dose profiles at the edges of the ablation zone, they found that adjusting thermal dose and thermal damage thresholds for thermal necrosis had a small, but statistically insignificant impact on the match between calculated and measured extents of the ablation zone. Shafirstein *et al.* [68] compared histologically observed extents of thermal necrosis following *in vivo* thermal ablation with a thermal conduction probe, with simulated thermal dose and thermal damage profiles. They found both thermal damage ($\Omega \geq 1$) and thermal dose ($t_{43} \geq 240$ min) thresholds to be in close agreement (< 2 mm) with observed histology, over a range of maximum probe temperatures.

Figures 8 and 9 show $T \geq 52$ °C, $t_{43} \geq 240$ min and $\Omega \geq 4.6$ isosurface clouds of sample treatment plans for thermal ablation with transurethral and interstitial applicators in a representative human prostate. For both treatment plans, extents of the predicted ablation zone as indicated by temperature, thermal dose and thermal damage isosurfaces are in close agreement. These models may be utilized by physicians in treatment planning prior to performing a treatment, to evaluate potential placement positions for the device to maximize the likelihood of complete ablation of the target zone while sparing surrounding critical structures. The sample patient-specific plans presented here illustrate the feasibility of treating targets in clinically relevant situations using interstitial and transurethral ultrasound applicators.

The models studied in this work may be used in conjunction with mathematical optimization techniques to optimize treatments plans for individual patients. Since mathematical optimization requires repeated calculation of the temperature profile for a given applicator configuration, model complexity of the speed of computation have to be traded off. Ablation

models based on temperature-dependent tissue properties require fewer computational resources than models based on thermal dose or thermal damage thresholds. In particular, adjusting tissue properties based on thermal dose or thermal damage requires more memory for storing the thermal dose/damage profile at all points in the computational domain, compared to models that adjust tissue properties on temperature. Thus, temperature-based models may be more suitable for treatment planning routines and model-based feedback control techniques that evaluate the temperature profile multiple times in order to evaluate an optimum configuration. More comprehensive models that adjust tissue properties based on thermal dose and damage may be more suitable in situations where fast computation is not essential.

One limitation of this study is that we only analyzed ultrasound applicators with tubular transducers, while neglecting planar and curvilinear (moderately curved) transducers. We note that planar and curvilinear transducers provide a more focused emission of acoustic energy, thereby depositing much larger amounts of acoustic energy close to the transducer. Based on results shown here for 90° sectored transducers versus 360° transducers, incorporating dynamic changes in tissue properties would be of even greater importance for these cases [57]. In this study, we focused on modeling catheter-based ultrasound ablation with temperature based feedback control, as would be applied in a practical setting. We implemented closed-loop control, using temperature information in sampling intervals that may be obtained from MR thermometry, to limit maximum tissue temperature.

Conclusion

Bioheat transfer models are a valuable tool for exploring device designs and treatment delivery strategies for thermal ablation devices. We have studied the impact of dynamic changes in tissue thermal and acoustic properties on the size of ablation zones estimated by bioheat transfer models with temperature based feedback control of interstitial and transurethral ultrasound applicators. There are considerable differences in computed sizes of ablation zones, safety margin, and maximum tissue temperatures, when employing tissue models that adjust acoustic attenuation and blood perfusion dynamically compared to those that to not adjust attenuation, even though, the specific model used to vary the properties are less consequential. We also performed a comparative analysis of several thermal damage models for assessing extents of the ablation zone. Results of this analysis demonstrate that for the 5—15 min thermal ablations typical with this modality, thermal damage and thermal dose measures are in good agreement with each other. Temperature thresholds may be used as indicators of treatment endpoint, however, careful attention must be given to the duration of the ablation. Since temperature is the quantity directly measured during treatments, knowledge of these temperature thresholds is of great practical value. Finally, we illustrate the implementation of these models for creating patient-specific treatment plans for thermal ablation treatments. These plans may be used in conjunction with numerical optimization strategies to determine optimal applicator positioning, orientation and power settings for individual treatments.

Acknowledgments

This work was supported by National Institute of Health grants R01CA122276, R01CA111981, R41CA121740, R44CA134169, and R21CA137472.

References

1. Webb H, Lubner MG, Hinshaw JL. Thermal ablation. Semin Roentgenol. 2011; 46(2):133–141. [PubMed: 21338838]

2. Ahmed M, Brace CL, Lee FT Jr, Goldberg SN. Principles of and advances in percutaneous ablation. Radiology. 2011; 258(2):351–369. [PubMed: 21273519]
3. Diederich CJ. Thermal ablation and high-temperature thermal therapy: Overview of technology and clinical implementation. Int J Hyperthermia. 2005; 21(8):745–753. [PubMed: 16338857]
4. Deardorff DL, Diederich CJ, Nau WH. Control of interstitial thermal coagulation: Comparative evaluation of microwave and ultrasound applicators. Med Phys. 2001; 28(1):104–117. [PubMed: 11213915]
5. Mougenot C, Quesson B, de Senneville BD, de Oliveira PL, Sprinkhuizen S, Palussiere J, et al. Three-dimensional spatial and temporal temperature control with mr thermometry-guided focused ultrasound (MRgHIFU). Magn Reson Med. 2009; 61(3):603–614. [PubMed: 19097249]
6. Rove KO, Sullivan KF, Crawford ED. High-intensity focused ultrasound: Ready for primetime. Urol Clin North Am. 2010; 37(1):27–35. [PubMed: 20152517]
7. Fischer K, Gedroyc W, Jolesz FA. Focused ultrasound as a local therapy for liver cancer. Cancer J. 2010; 16(2):118–124. [PubMed: 20404608]
8. Uchida T, Sanghvi NT, Gardner TA, Koch MO, Ishii D, Minei S, et al. Transrectal high-intensity focused ultrasound for treatment of patients with stage T1b-2n0m0 localized prostate cancer: A preliminary report. Urology. 2002; 59(3):394–398. [PubMed: 11880077]
9. Tanter M, Pernot M, Aubry JF, Montaldo G, Marquet F, Fink M. Compensating for bone interfaces and respiratory motion in high-intensity focused ultrasound. Int J Hyperthermia. 2007; 23(2):141–151. [PubMed: 17578338]
10. Nau WH, Diederich CJ, Simko J, Juang T, Jacoby A, Burdette EC. Ultrasound interstitial thermal therapy (USITT) for the treatment of uterine myomas. Proc SPIE 6440. 2007
11. Diederich CJ, Nau WH, Ross AB, Tyreus PD, Butts K, Rieke V, et al. Catheter-based ultrasound applicators for selective thermal ablation: Progress towards MRI-guided applications in prostate. Int J Hyperthermia. 2004; 20(7):739–756. [PubMed: 15675669]
12. Lafon C, Melodelima D, Salomir R, Chapelon JY. Interstitial devices for minimally invasive thermal ablation by high-intensity ultrasound. Int J Hyperthermia. 2007; 23(2):153–163. [PubMed: 17578339]
13. Nau WH, Diederich CJ, Burdette EC. Evaluation of multielement catheter-cooled interstitial ultrasound applicators for high-temperature thermal therapy. Med Phys. 2001; 28(7):1525–1534. [PubMed: 11488586]
14. Chopra R, Baker N, Choy V, Boyes A, Tang K, Bradwell D, et al. MRI-compatible transurethral ultrasound system for the treatment of localized prostate cancer using rotational control. Med Phys. 2008; 35(4):1346–1357. [PubMed: 18491529]
15. Kinsey AM, Diederich CJ, Rieke V, Nau WH, Pauly KB, Bouley D, et al. Transurethral ultrasound applicators with dynamic multi-sector control for prostate thermal therapy: In vivo evaluation under MR guidance. Med Phys. 2008; 35(5):2081–2093. [PubMed: 18561684]
16. Nau WH, Diederich CJ, Shu R, Kinsey A, Bass E, Lotz J, et al. Intradiscal thermal therapy using interstitial ultrasound: An in vivo investigation in ovine cervical spine. Spine (Phila Pa 1976). 2007; 32(5):503–511. [PubMed: 17334283]
17. Ross AB, Diederich CJ, Nau WH, Rieke V, Butts RK, Sommer G, et al. Curvilinear transurethral ultrasound applicator for selective prostate thermal therapy. Med Phys. 2005; 32(6):1555–1565. [PubMed: 16013714]
18. Seket B, Lafon C, Mithieux F, Goldenstedt C, Paquet C, Chapelon JY, et al. Developing an interstitial ultrasound applicator for thermal ablation in liver: Results of animal experiments. J Surg Res. 2007; 142(1):81–89. [PubMed: 17716609]
19. Delabrousse E, Mithieux F, Birer A, Salomir R, Chapelon J, Lafon C. Ultrasound interstitial mini invasive probes for thermal ablation in liver: Feasibility study in vivo. J Radiol. 2007; 88(11 Pt 2): 1817–1822. [PubMed: 18065946]
20. Chopra R, Tang K, Burtnyk M, Boyes A, Sugar L, Appu S, et al. Analysis of the spatial and temporal accuracy of heating in the prostate gland using transurethral ultrasound therapy and active MR temperature feedback. Phys Med Biol. 2009; 54(9):2615–2633. [PubMed: 19351975]

21. Schumann C, Rieder C, Bieberstein J, Weihusen A, Zidowitz S, Moltz JH, et al. State of the art in computer-assisted planning, intervention, and assessment of liver-tumor ablation. Crit Rev Biomed Eng. 2010; 38(1):31–52. [PubMed: 21175402]
22. Chen CC, Miga MI, Galloway RL Jr. Optimizing electrode placement using finite-element models in radiofrequency ablation treatment planning. IEEE Trans Biomed Eng. 2009; 56(2):237–245. [PubMed: 19272862]
23. Zhai W, Xu J, Zhao Y, Song Y, Sheng L, Jia P. Preoperative surgery planning for percutaneous hepatic microwave ablation. Med Image Comput Comput Assist Interv. 2008; 11(Pt 2):569–577. [PubMed: 18982650]
24. Wan H, Aarsvold J, O'Donnell M, Cain C. Thermal dose optimization for ultrasound tissue ablation. IEEE Trans Ultrason Ferroelectr Freq Control. 1999; 46(4):913–928. [PubMed: 18238496]
25. Fuentes D, Cardan R, Stafford RJ, Yung J, Dodd GD 3rd, Feng Y. High-fidelity computer models for prospective treatment planning of radiofrequency ablation with in vitro experimental correlation. J Vasc Interv Radiol. 2010; 21(11):1725–1732. [PubMed: 20920840]
26. Garnier C, Lafon C, Dillenseger JL. 3-D modeling of the thermal coagulation necrosis induced by an interstitial ultrasonic transducer. IEEE Trans Biomed Eng. 2008; 55(2 Pt 2):833–837. [PubMed: 18270029]
27. Damianou C, Hynynen K. The effect of various physical parameters on the size and shape of necrosed tissue volume during ultrasound surgery. J Acoust Soc Am. 1994; 95(3):1641–1649. [PubMed: 8176064]
28. Mast TD, Makin IR, Faidi W, Runk MM, Barthe PG, Slayton MH. Bulk ablation of soft tissue with intense ultrasound: Modeling and experiments. J Acoust Soc Am. 2005; 118(4):2715–2724. [PubMed: 16266191]
29. Schutt DJ, Haemmerich D. Effects of variation in perfusion rates and of perfusion models in computational models of radio frequency tumor ablation. Med Phys. 2008; 35(8):3462–3470. [PubMed: 18777906]
30. Clarke RL, Bush NL, ter Haar GR. The changes in acoustic attenuation due to in vitro heating. Ultrasound Med Biol. 2003; 29(1):127–135. [PubMed: 12604124]
31. Damianou CA, Sanghvi NT, Fry FJ, Maass-Moreno R. Dependence of ultrasonic attenuation and absorption in dog soft tissues on temperature and thermal dose. J Acoust Soc Am. 1997; 102(1): 628–634. [PubMed: 9228822]
32. Worthington AE, Trachtenberg J, Sherar MD. Ultrasound properties of human prostate tissue during heating. Ultrasound Med Biol. 2002; 28(10):1311–1318. [PubMed: 12467858]
33. Tyreus PD, Diederich C. Two-dimensional acoustic attenuation mapping of high-temperature interstitial ultrasound lesions. Phys Med Biol. 2004; 49(4):533–546. [PubMed: 15005163]
34. Bhattacharya A, Mahajan RL. Temperature dependence of thermal conductivity of biological tissues. Physiol Meas. 2003; 24(3):769–783. [PubMed: 14509313]
35. Valvano JW, Cochran JR, Diller KR. Thermal conductivity and diffusivity of biomaterials measured with self-heated thermistors. Int J Thermophys. 1985; 6(3):301–311.
36. van Vulpen M, Raaymakers BW, de Leeuw AA, van de Kamer JB, van Moorselaar RJ, Hobbelink MG, et al. Prostate perfusion in patients with locally advanced prostate carcinoma treated with different hyperthermia techniques. J Urol. 2002; 168(4 Pt 1):1597–1602. [PubMed: 12352464]
37. He X, McGee S, Coad JE, Schmidlin F, Iaizzo PA, Swanlund DJ, et al. Investigation of the thermal and tissue injury behaviour in microwave thermal therapy using a porcine kidney model. Int J Hyperthermia. 2004; 20(6):567–593. [PubMed: 15370815]
38. Kruskal JB, Oliver B, Huertas JC, Goldberg SN. Dynamic intrahepatic flow and cellular alterations during radiofrequency ablation of liver tissue in mice. J Vasc Interv Radiol. 2001; 12(10):1193–1201. [PubMed: 11585886]
39. Bouchoux G, Lafon C, Berriet R, Chapelon JY, Fleury G, Cathignol D. Dual-mode ultrasound transducer for image-guided interstitial thermal therapy. Ultrasound Med Biol. 2008; 34(4):607–616. [PubMed: 18055099]

40. Owen NR, Bouchoux G, Seket B, Murillo-Rincon A, Merouche S, Birer A, et al. In vivo evaluation of a mechanically oscillating dual-mode applicator for ultrasound imaging and thermal ablation. IEEE Trans Biomed Eng. 2010; 57(1):80–92. [PubMed: 19497808]
41. Chopra R, Wachsmuth J, Burtnyk M, Haider MA, Bronskill MJ. Analysis of factors important for transurethral ultrasound prostate heating using MR temperature feedback. Phys Med Biol. 2006; 51(4):827–844. [PubMed: 16467581]
42. Sinelnikov YD, Fjield T, Sapozhnikov OA. The mechanism of lesion formation by focused ultrasound ablation catheter for treatment of atrial fibrillation. Acoust Phys. 2009; 55(4–5):647–656. [PubMed: 20161431]
43. Lafon C, Prat F, Chapelon JY, Gorry F, Margonari J, Theillere Y, et al. Cylindrical thermal coagulation necrosis using an interstitial applicator with a plane ultrasonic transducer: In vitro and in vivo experiments versus computer simulations. Int J Hyperthermia. 2000; 16(6):508–522. [PubMed: 11129262]
44. Skinner MG, Iizuka MN, Kolios MC, Sherar MD. A theoretical comparison of energy sources--microwave, ultrasound and laser--for interstitial thermal therapy. Phys Med Biol. 1998; 43(12): 3535–3547. [PubMed: 9869030]
45. Burtnyk M, Chopra R, Bronskill MJ. Quantitative analysis of 3-D conformal MRI-guided transurethral ultrasound therapy of the prostate: Theoretical simulations. Int J Hyperthermia. 2009; 25(2):116–131. [PubMed: 19337912]
46. Connor CW, Hynynen K. Bio-acoustic thermal lensing and nonlinear propagation in focused ultrasound surgery using large focal spots: A parametric study. Phys Med Biol. 2002; 47(11): 1911–1928. [PubMed: 12108775]
47. Watkin NA, ter Haar GR, Rivens I. The intensity dependence of the site of maximal energy deposition in focused ultrasound surgery. Ultrasound Med Biol. 1996; 22(4):483–491. [PubMed: 8795175]
48. Sapareto SA, Dewey WC. Thermal dose determination in cancer therapy. Int J Radiat Oncol Biol Phys. 1984; 10(6):787–800. [PubMed: 6547421]
49. Henriques FC Jr. Studies of thermal injury; the predictability and the significance of thermally induced rate processes leading to irreversible epidermal injury. Arch Pathol (Chic). 1947; 43(5): 489–502.
50. Lepetit-Coiffe M, Laumonier H, Seror O, Quesson B, Sesay MB, Moonen CT, et al. Real-time monitoring of radiofrequency ablation of liver tumors using thermal-dose calculation by MRI temperature imaging: Initial results in nine patients, including follow-up. Eur Radiol. 2010; 20(1): 193–201. [PubMed: 19657650]
51. Siddiqui K, Chopra R, Vedula S, Sugar L, Haider M, Boyes A, et al. MRI-guided transurethral ultrasound therapy of the prostate gland using real-time thermal mapping: Initial studies. Urology. 2010; 76:1506–1511. [PubMed: 20709381]
52. Enholm JK, Kohler MO, Quesson B, Mougenot C, Moonen CT, Sokka SD. Improved volumetric MR-HIFU ablation by robust binary feedback control. IEEE Trans Biomed Eng. 2010; 57(1):103–113. [PubMed: 19846364]
53. Ross AB, Diederich CJ, Nau WH, Gill H, Bouley DM, Daniel B, et al. Highly directional transurethral ultrasound applicators with rotational control for MRI-guided prostatic thermal therapy. Phys Med Biol. 2004; 49(2):189–204. [PubMed: 15083666]
54. Diederich CJ, Burdette EC. Transurethral ultrasound array for prostate thermal therapy: Initial studies. IEEE Trans Ultrason Ferroelectr Freq Control. 1996; 43(6):1011–1022.
55. Diederich CJ, Nau WH, Stauffer PR. Ultrasound applicators for interstitial thermal coagulation. IEEE Trans Ultrason Ferroelectr Freq Control. 1999; 46(5):1218–1228. [PubMed: 18244315]
56. Tyreus PD, Diederich CJ. Theoretical model of internally cooled interstitial ultrasound applicators for thermal therapy. Phys Med Biol. 2002; 47(7):1073–1089. [PubMed: 11996056]
57. Wootton JH, Ross AB, Diederich CJ. Prostate thermal therapy with high intensity transurethral ultrasound: The impact of pelvic bone heating on treatment delivery. Int J Hyperthermia. 2007; 23(8):609–622. [PubMed: 18097849]
58. Pennes H. Analysis of tissue and arterial blood temperatures in the resting human forearm. Journal of Applied Physiology. 1948; 1(2):93–122. [PubMed: 18887578]

59. Diederich CJ, Hynynen K. The development of intracavitary ultrasonic applicators for hyperthermia: A design and experimental study. Med Phys. 1990; 17(4):626–634. [PubMed: 2215407]
60. Rieke V, Butts Pauly K. MR thermometry. J Magn Reson Imaging. 2008; 27(2):376–390. [PubMed: 18219673]
61. Dewhirst MW, Viglianti BL, Lora-Michiels M, Hanson M, Hoopes PJ. Basic principles of thermal dosimetry and thermal thresholds for tissue damage from hyperthermia. Int J Hyperthermia. 2003; 19(3):267–294. [PubMed: 12745972]
62. Dewey WC. Arrhenius relationships from the molecule and cell to the clinic. International Journal of Hyperthermia. 1994; 10(4):457–483. [PubMed: 7963805]
63. Agah R, Pearce JA, Welch AJ, Motamedi M. Rate process model for arterial tissue thermal damage: Implications on vessel photocoagulation. Lasers Surg Med. 1994; 15(2):176–184. [PubMed: 7799743]
64. Rylander MN, Feng Y, Zimmermann K, Diller KR. Measurement and mathematical modeling of thermally induced injury and heat shock protein expression kinetics in normal and cancerous prostate cells. Int J Hyperthermia. 2010; 26(8):748–764. [PubMed: 20858083]
65. Breen MS, Breen M, Butts K, Chen L, Saidel GM, Wilson DL. MRI-guided thermal ablation therapy: Model and parameter estimates to predict cell death from mr thermometry images. Ann Biomed Eng. 2007; 35(8):1391–1403. [PubMed: 17436111]
66. He X, Bhowmick S, Bischof JC. Thermal therapy in urologic systems: A comparison of arrhenius and thermal isoeffective dose models in predicting hyperthermic injury. J Biomech Eng. 2009; 131(7) 074507.
67. Thomsen S, Pearce JA, Cheong WF. Changes in birefringence as markers of thermal damage in tissues. IEEE Trans Biomed Eng. 1989; 36(12):1174–1179. [PubMed: 2606492]
68. Shafirstein G, Novak P, Moros EG, Siegel E, Hennings L, Kaufmann Y, et al. Conductive interstitial thermal therapy device for surgical margin ablation: In vivo verification of a theoretical model. Int J Hyperthermia. 2007; 23(6):477–492. [PubMed: 17852514]
69. Pearce, JA.; Thomsen, S. Rate process analysis of thermal damage. In: Welch, AJ.; van Gemert, MJC., editors. Optical-Thermal response of Laser Irradiated Tissue. New York: Plenum Press; 1995. p. 561-606.
70. Borrelli MJ, Thompson LL, Cain CA, Dewey WC. Time-temperature analysis of cell killing of BHK cells heated at temperatures in the range of 43.5 degrees C to 57.0 degrees C. Int J Radiat Oncol Biol Phys. 1990; 19(2):389–399. [PubMed: 2394618]
71. Boyes A, Tang K, Yaffe M, Sugar L, Chopra R, Bronskill M. Prostate tissue analysis immediately following magnetic resonance imaging guided transurethral ultrasound thermal therapy. J Urol. 2007; 178(3 Pt 1):1080–1085. [PubMed: 17644137]
72. McDannold N, Hynynen K, Wolf D, Wolf G, Jolesz F. MRI evaluation of thermal ablation of tumors with focused ultrasound. J Magn Reson Imaging. 1998; 8(1):91–100. [PubMed: 9500266]
73. Pearce JA. Relationship between arrhenius models of thermal damage and the CEM 43 thermal dose. Proc SPIE 7181. 2009
74. Pauly KB, Diederich CJ, Rieke V, Bouley D, Chen J, Nau WH, et al. Magnetic resonance-guided high-intensity ultrasound ablation of the prostate. Top Magn Reson Imaging. 2006; 17(3):195–207. [PubMed: 17414077]
75. Yung JP, Shetty A, Elliott A, Weinberg JS, McNichols RJ, Gowda A, et al. Quantitative comparison of thermal dose models in normal canine brain. Med Phys. 2010; 37(10):5313–5321. [PubMed: 21089766]
76. Song CW. Effect of local hyperthermia on blood flow and microenvironment: A review. Cancer Res. 1984; 44(10 Suppl):4721s–4730s. [PubMed: 6467226]
77. Song CW, Lokshina A, Rhee JG, Patten M, Levitt SH. Implication of blood flow in hyperthermic treatment of tumors. IEEE Trans Biomed Eng. 1984; 31(1):9–16. [PubMed: 6724614]
78. Buy X, Tok CH, Szwarc D, Bierry G, Gangi A. Thermal protection during percutaneous thermal ablation procedures: Interest of carbon dioxide dissection and temperature monitoring. Cardiovasc Intervent Radiol. 2009; 32(3):529–534. [PubMed: 19219496]

79. Yarmolenko PS, Moon EJ, Landon C, Manzoor A, Hochman DW, Viglianti BL, et al. Thresholds for thermal damage to normal tissues: An update. Int J Hyperthermia. 2011; 27(4):320–343. [PubMed: 21591897]

80. McDannold N, Tempany C, Jolesz F, Hynynen K. Evaluation of referenceless thermometry in MRI-guided focused ultrasound surgery of uterine fibroids. J Magn Reson Imaging. 2008; 28(4): 1026–1032. [PubMed: 18821603]

81. Kangasniemi M, Diederich CJ, Price RE, Stafford RJ, Schomer DF, Olsson LE, et al. Multiplanar MR temperature-sensitive imaging of cerebral thermal treatment using interstitial ultrasound applicators in a canine model. J Magn Reson Imaging. 2002; 16(5):522–531. [PubMed: 12412028]

82. Hazle JD, Diederich CJ, Kangasniemi M, Price RE, Olsson LE, Stafford RJ. MRI-guided thermal therapy of transplanted tumors in the canine prostate using a directional transurethral ultrasound applicator. J Magn Reson Imaging. 2002; 15(4):409–417. [PubMed: 11948830]

83. Nau WH, Diederich CJ, Ross AB, Butts K, Rieke V, Bouley DM, et al. MRI-guided interstitial ultrasound thermal therapy of the prostate: A feasibility study in the canine model. Med Phys. 2005; 32(3):733–743. [PubMed: 15839345]

84. Duck, F. Physical properties of tissue: A comprehensive reference book. London: Academic Press; 1990.

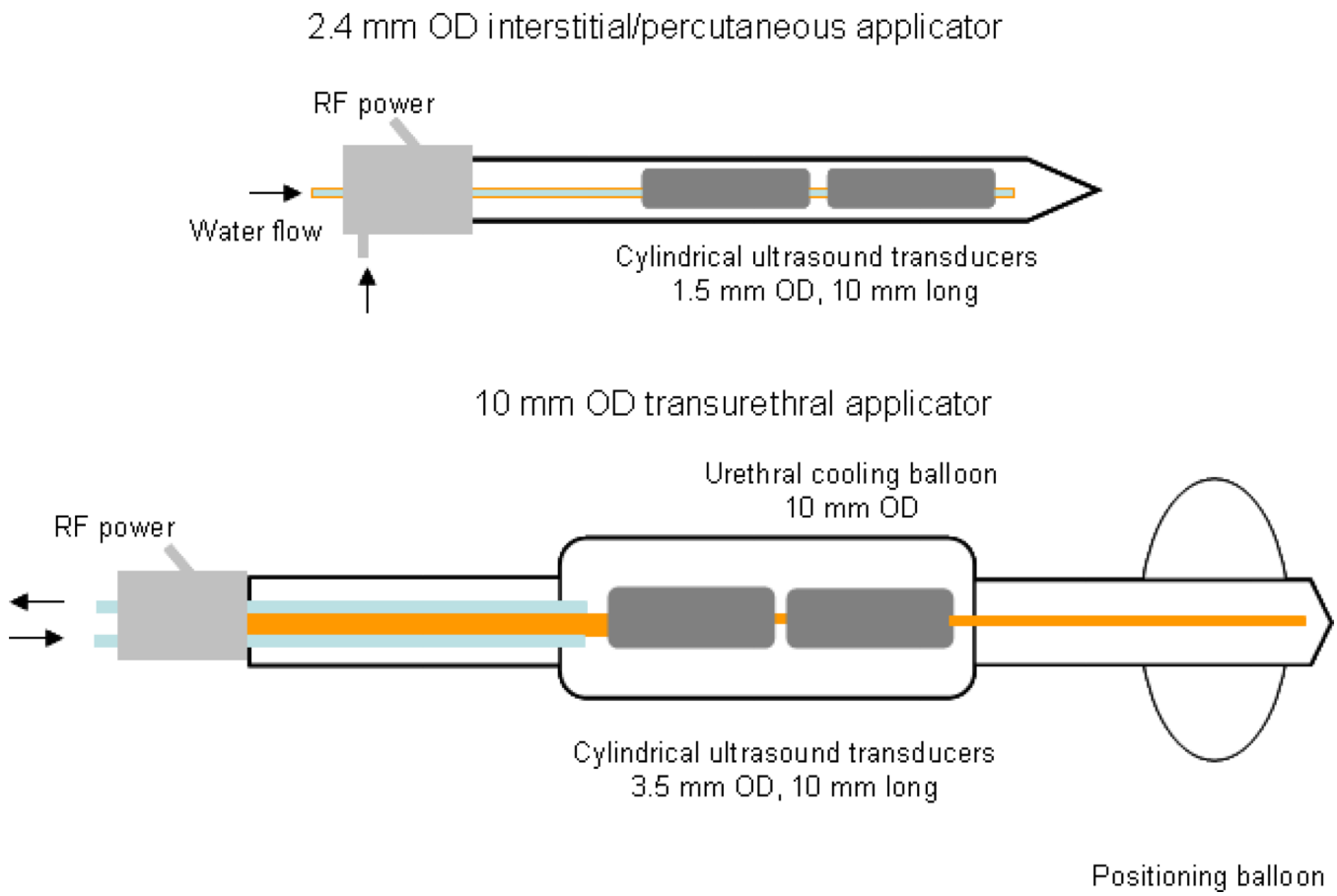

Figure 1.
Catheter-based ultrasound applicators with tubular transducer segments for thermal ablation: (top) 2.4 mm OD applicator suitable for interstitial or percutaneous ablation of prostate and liver targets, (bottom) 10 mm OD transurethral applicator for ablation of prostate targets. Transducers may be modified to sonicate in 90°, 180°, or 270° sectors of the angular expanse, or left unmodified for 360° sonication. (Not to scale).

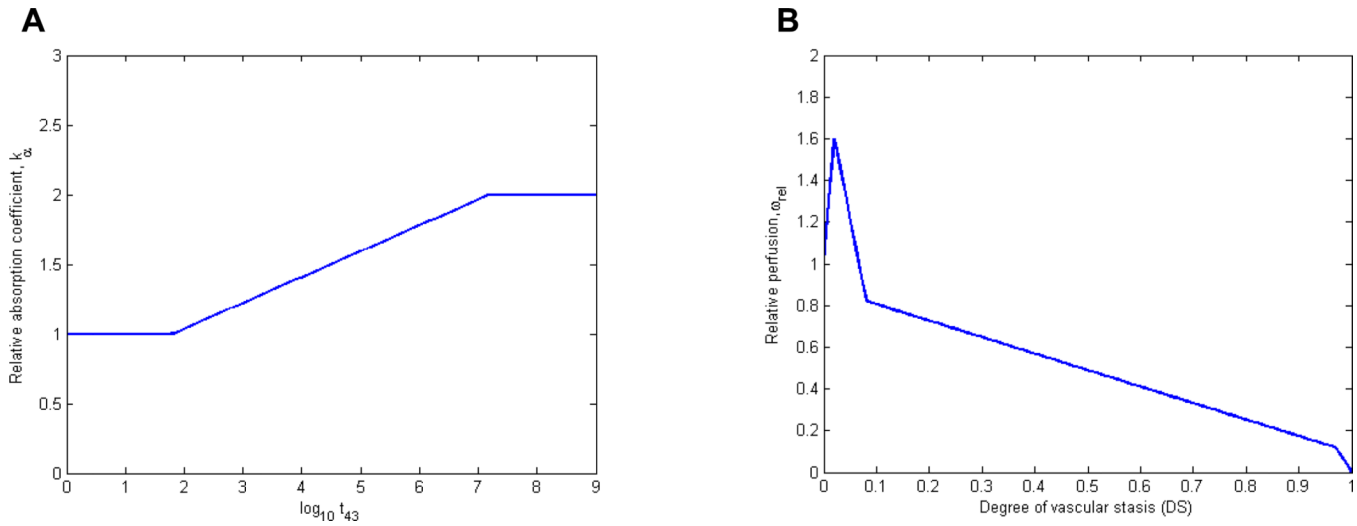

Figure 2.

(a) Acoustic attenuation coefficient, $\alpha = k_\alpha \alpha_0$, increases linearly with the logarithm of thermal dose, t_{43}, as described in [31] and employed in models 1—3 (b) Blood mass perfusion rate $\dot{m}_{bl} = \dot{m}_{0,bl}\dot{m}_{rel}$, varies as a function of degree of vascular stasis, computed using an Arrhenius model, as described in [29] and [37] and employed in model 1.

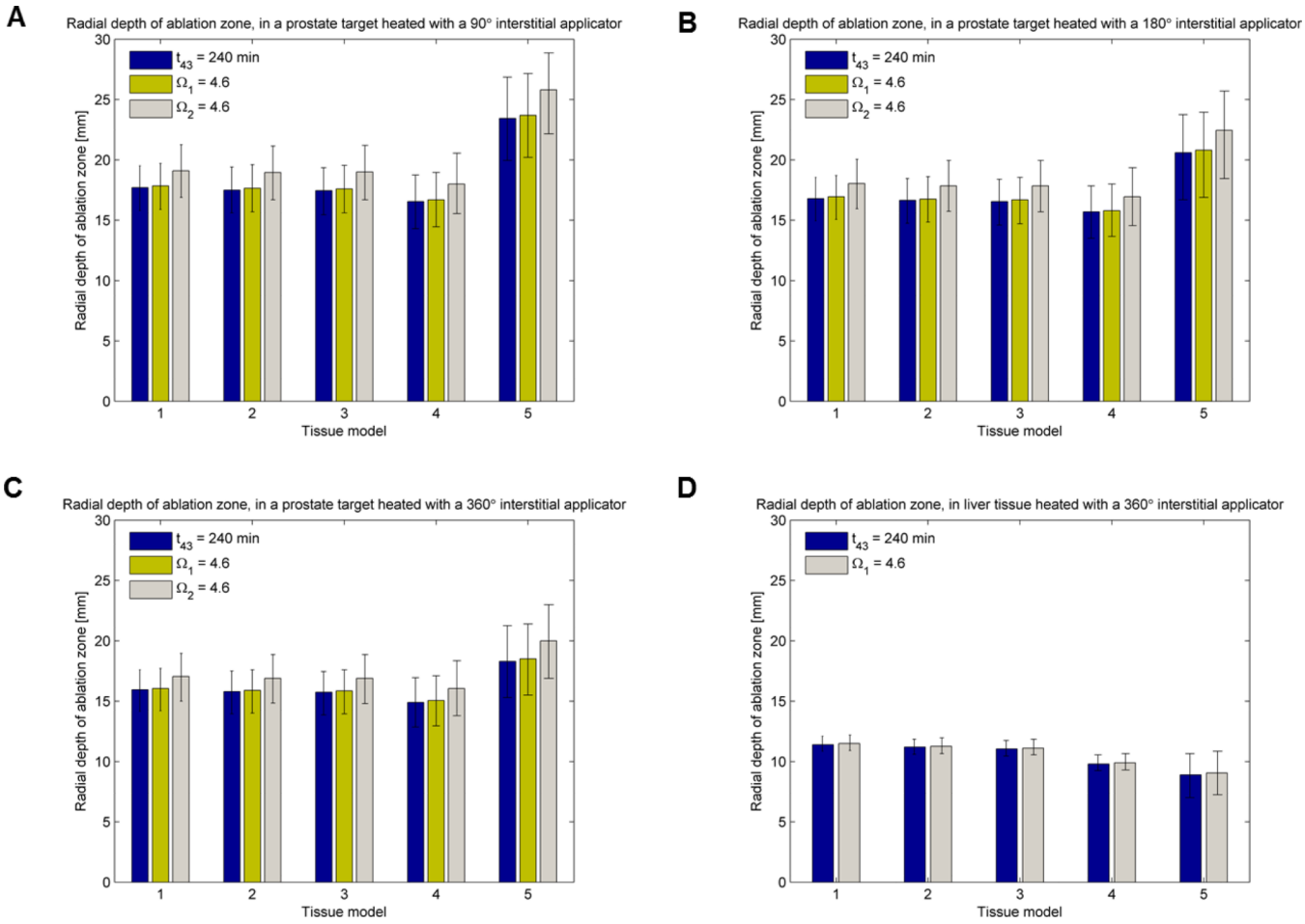

Figure 3.

Radial depth of ablation zone after 15 min ablations in prostate and liver targets using interstitial applicators as predicted by thermal dose (t_{43}) and thermal damage (Ω_1 uses Arrhenius parameters reported in [66] and Ω_2 uses parameters reported in [70]) indicators. Error bars indicate ranges computed using higher (5 kg m^{-3} s^{-1} in prostate, 20 kg m^{-3} s^{-1} in liver) and lower (1 kg m−3 s−1 and 10 kg m^{-3} s^{-1}) values for the nominal (2.5 kg m^{-3} s^{-1} in prostate, 15 kg m^{-3} s^{-1} in liver) blood perfusion rate. (a) 360° applicator in prostate (b) 180° applicator in prostate (c) 90° applicator in prostate and (d) 360° applicator in liver.

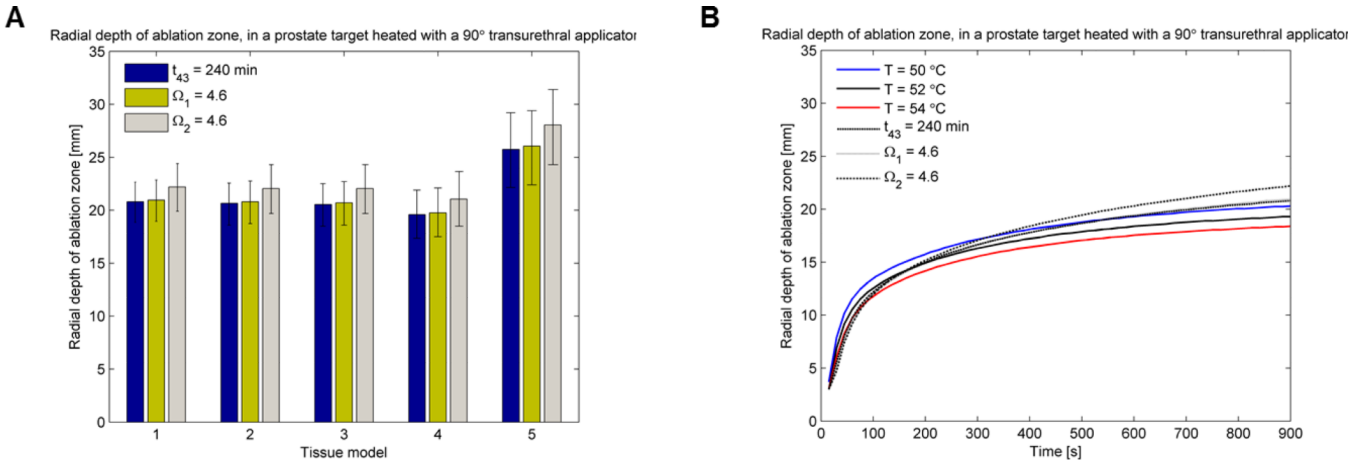

Figure 4.

(a) Radial depth of ablation zone after 15 min prostate ablations with a 90° transurethral applicator, as predicted by thermal dose (t_{43}) and thermal damage (Ω_1 uses Arrhenius parameters reported in [66] and Ω_2 uses parameters reported in [70]) indicators (b) Radial depth of the ablation zone as indicated by temperature, thermal dose (t_{43}) and thermal damage (Ω_1 and Ω_2) thresholds, over the course of a 15 min ablation with a 90° transurethral applicator in prostate and liver tissue.

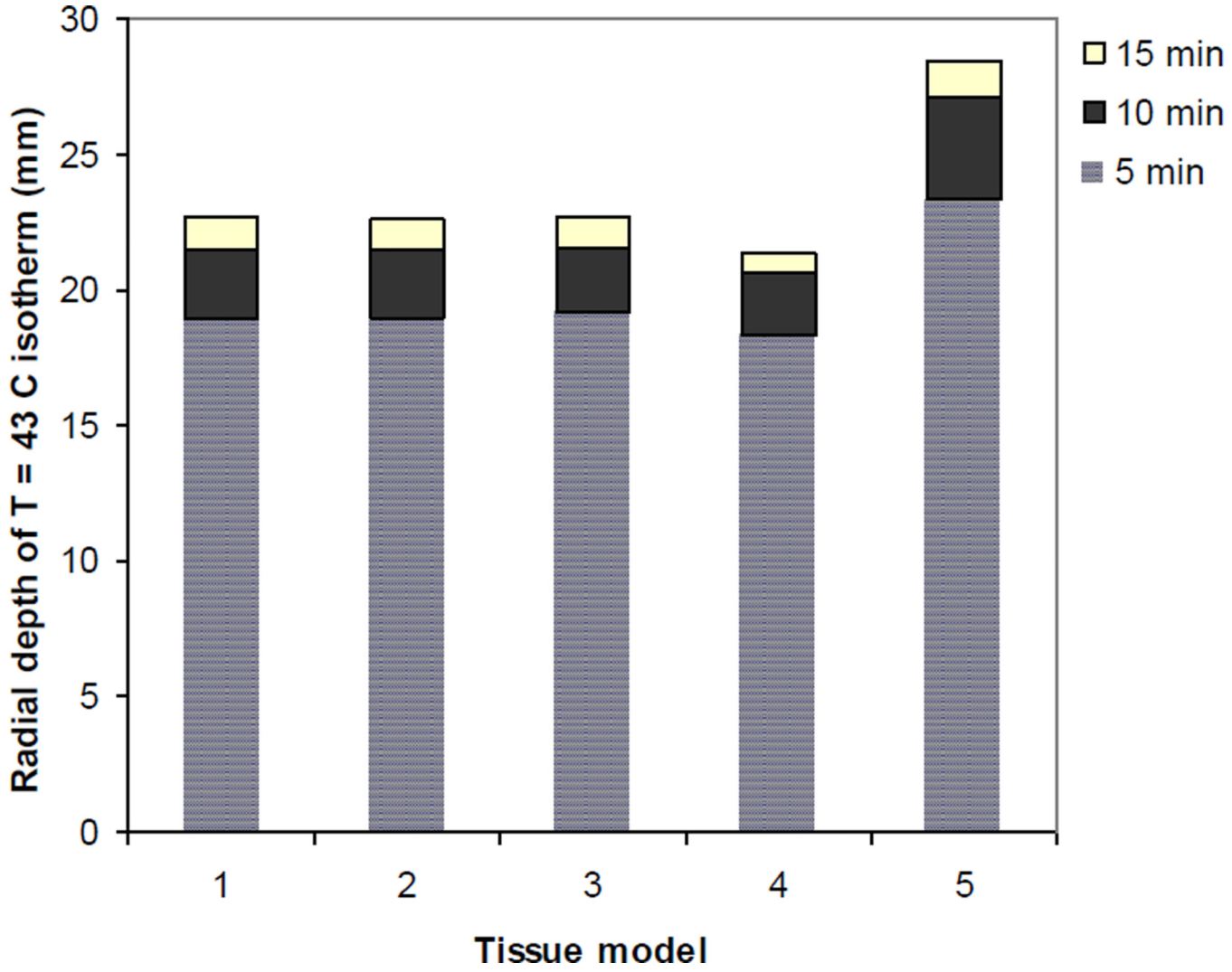

Figure 5.
Radial depth of the extents of thermal toxicity, as indicated by T = 43 °C isotherm, after 5—15 min thermal ablations with a 180° interstitial applicator in prostate target, simulated using tissue models 1—5.

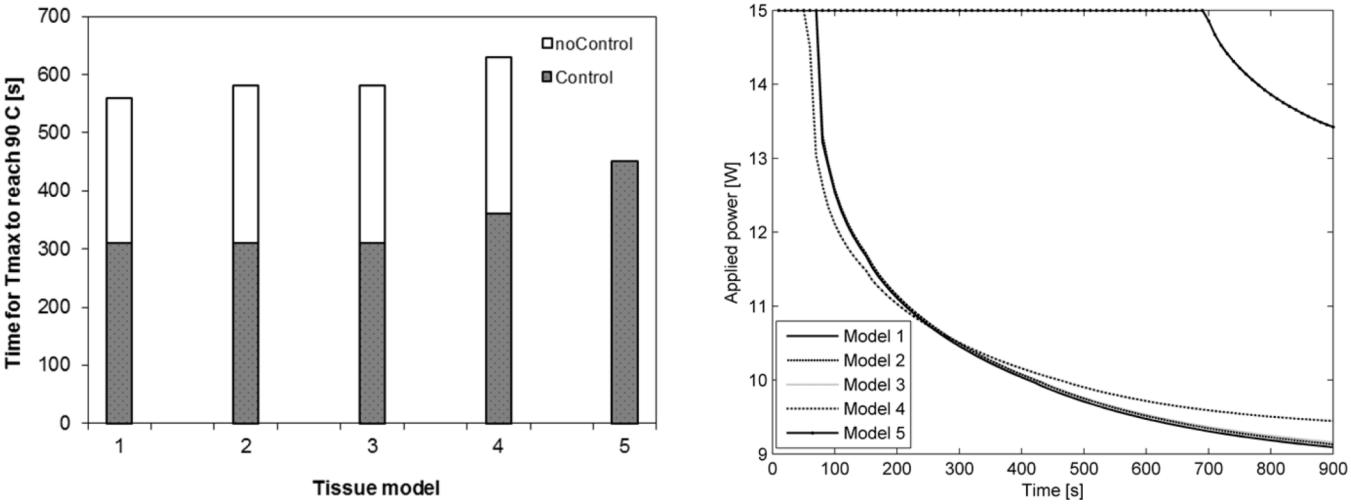

Figure 6.

(a) Transient evolution of maximum tissue temperature during 15 min ablations (with and without feedback control) using a 180° interstitial applicator in a prostate target. (b) Transient evolution of power applied to a 180° ultrasound sector as determined by the control algorithm simulated using tissue models 1—5.

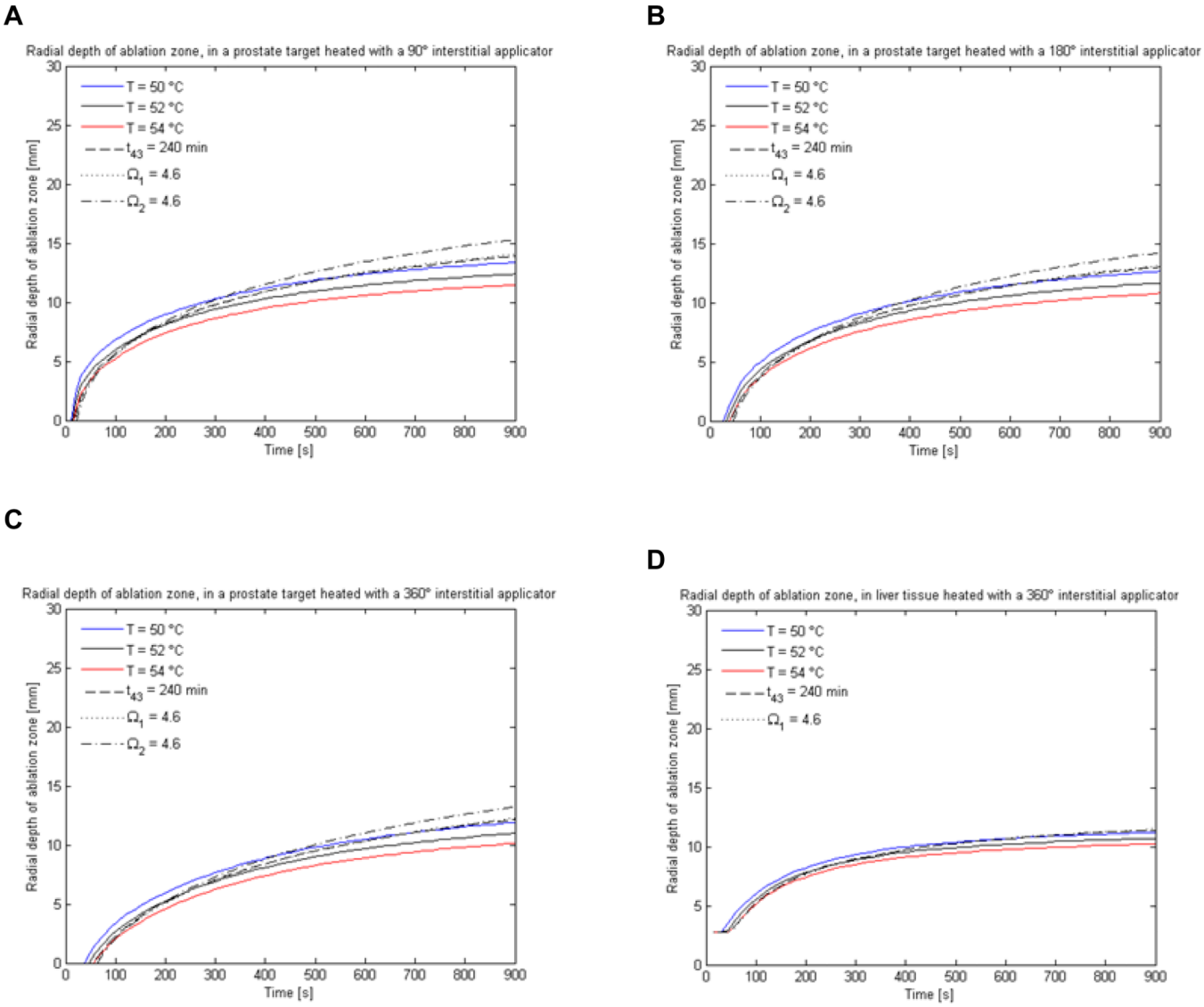

Figure 7.

Radial depth of the ablation zone as indicated by temperature, thermal dose (t_{43}) and thermal damage (Ω_1 and Ω_2) thresholds, over the course of a 15 min ablation with interstitial applicators in prostate and liver tissue. (a) 360° applicator in prostate (b) 180° applicator in prostate (c) 90° applicator prostate and (d) 360° applicator in liver.

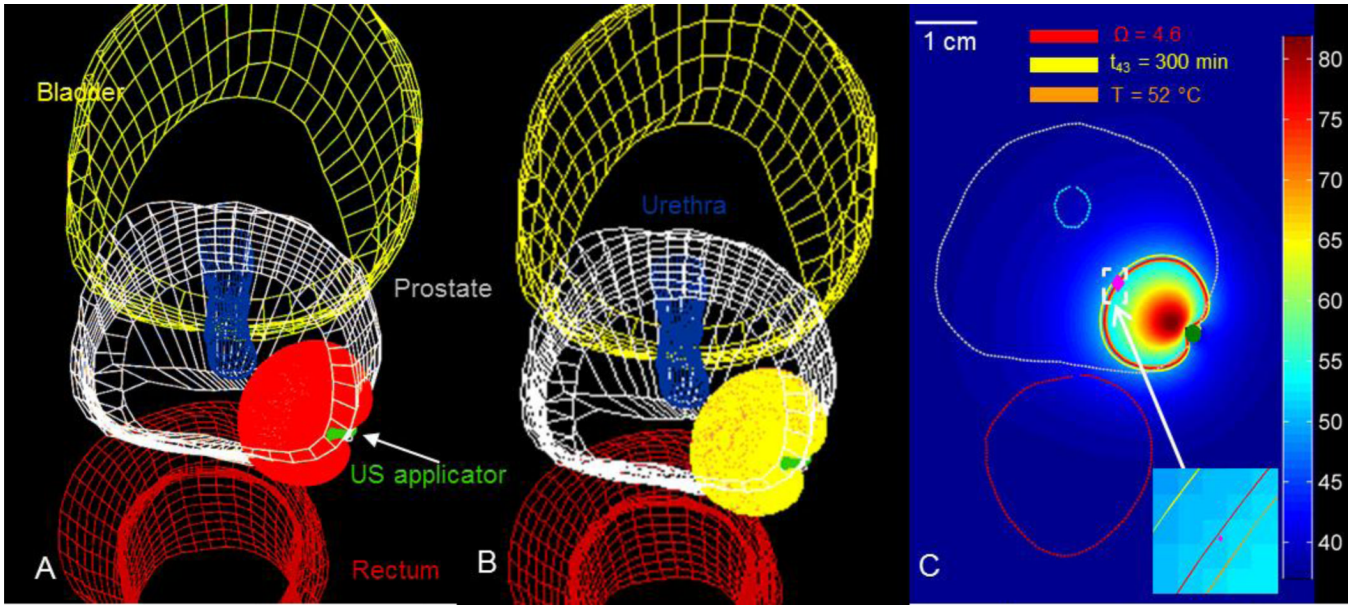

Figure 8.

Patient-specific treatment simulation and plan for targeting prostate cancer in the posterior gland using a directional (90°) interstitial ultrasound applicator, implanted in the peripheral gland and directed toward the urethra; (a) thermal damage ($\Omega \geq 4.6$) and temperature ($T \geq 52$ °C) isosurfaces indicating coagulative necrosis, (b) thermal dose ($t_{43} \geq 240$ min) and temperature ($T \geq 52$ °C) isosurfaces indicating coagulative necrosis, (c) temperature map in axial slice through the center of the applicator with critical temperature, thermal dose and thermal damage contours overlaid.

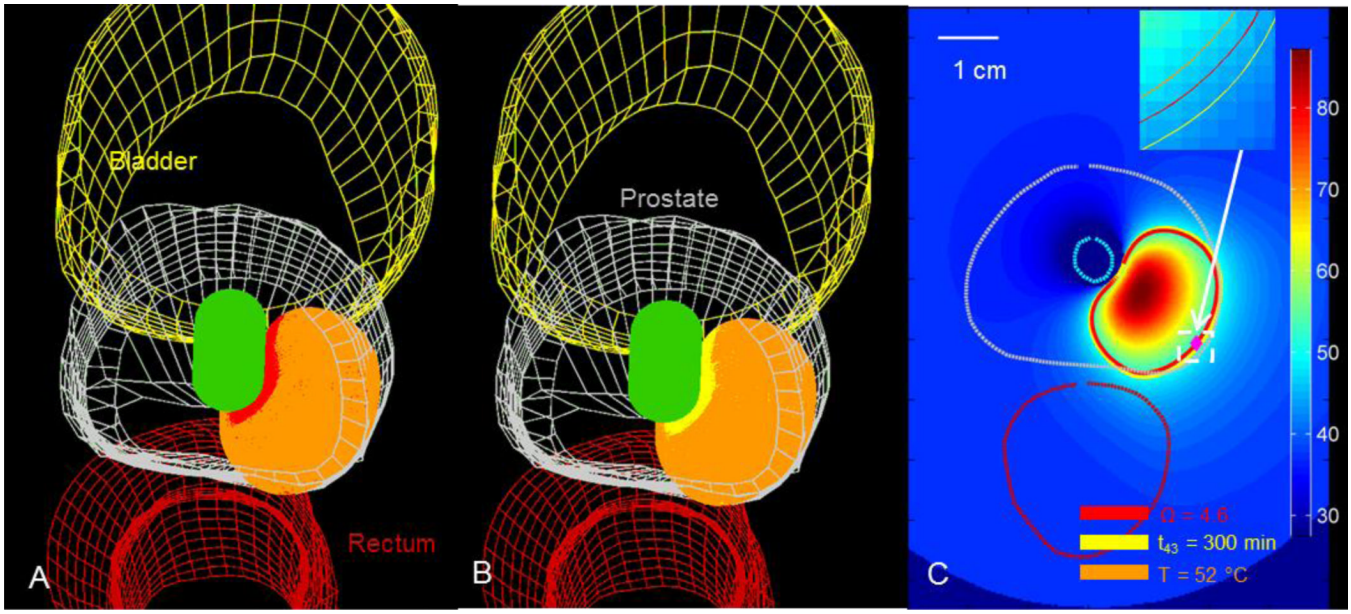

Figure 9.

Patient-specific treatment simulation and plan for targeting focal prostate cancer in the posterior gland using a directional (90°) transurethral ultrasound applicator directing energy toward the periphery; (a) thermal damage ($\Omega \geq 4.6$) and temperature ($T \geq 52$ °C) isosurfaces indicating coagulative necrosis, (b) thermal dose ($t_{43} \geq 240$ min) and temperature ($T \geq 52$ °C) isosurfaces indicating coagulative necrosis, (c) temperature map in axial slice through the center of the applicator with critical temperature, thermal dose, and thermal damage contours overlaid.

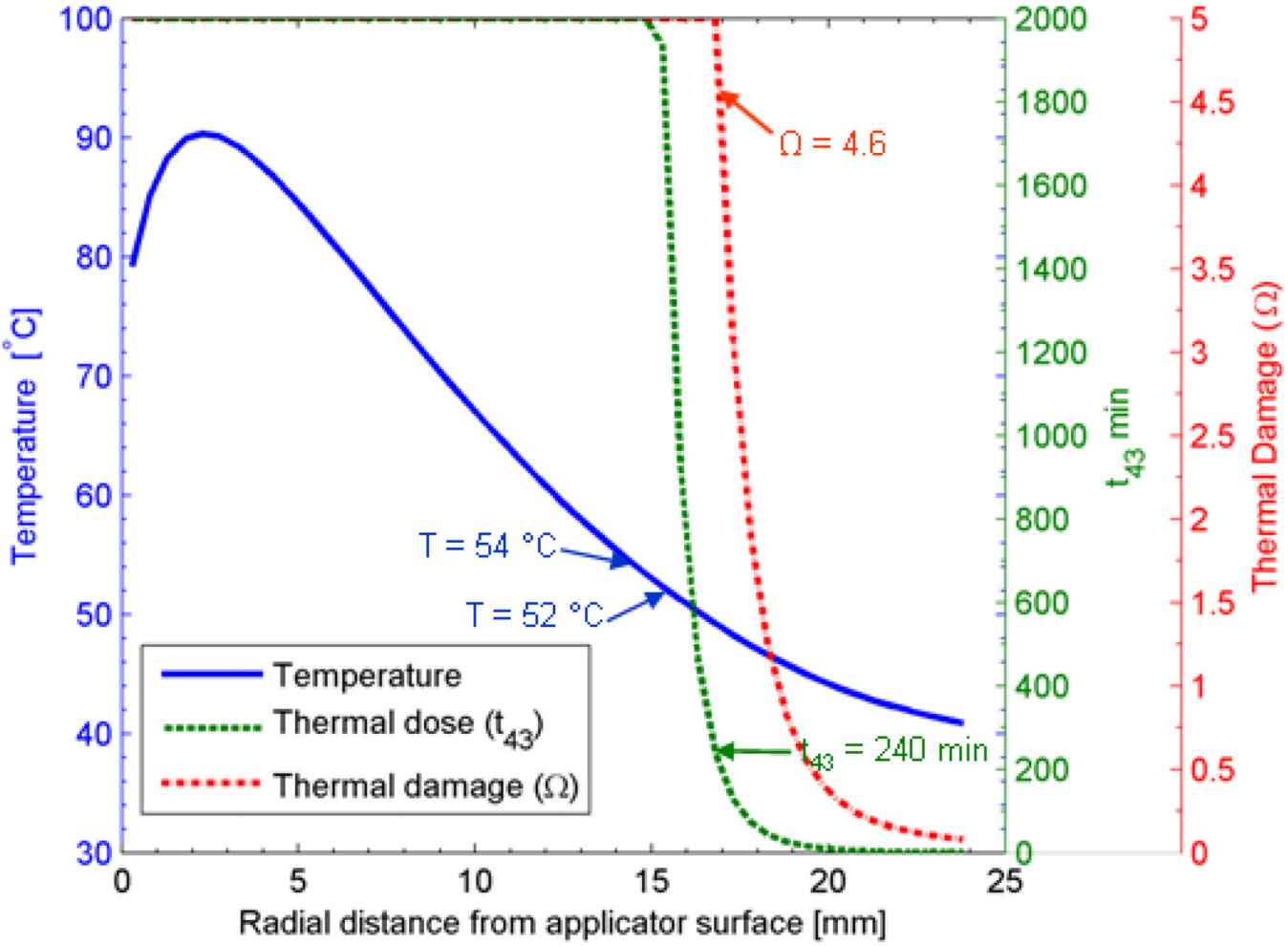

Figure 10.

Simulated temperature, thermal dose (t_{43}), and thermal damage (Ω) profiles after 15 min ablation with a 180° interstitial applicator in prostate tissue, showing sharp fall off of thermal dose and thermal damage profiles in regions close the boundary of the ablation zone.

Table I

Nominal values for tissue physical properties and model parameters.

Property	Symbol	Value		Units	Reference
		Prostate	*Liver*		
Density	ρ	1050	1050	kg m^{-3}	[84]
Specific heat capacity	c	3639	3639	J kg^{-1} K^{-1}	[84]
Thermal conductivity	k_0	0.54	0.51	W m^{-1} K^{-1}	[84]
Nominal blood perfusion rate	$\dot{m}_0$	2.5 (1—5)	15 (12–18)	kg m^{-3} s^{-1}	[84]
Nominal acoustic attenuation coefficient	μ_0	5.3	4.5	Np m^{-1} MHz^{-1}	[31, 32, 57]
Nominal acoustic absorption coefficient	α_0	5.3	4.5	Np m^{-1} MHz^{-1}	[31, 32, 57]
Activation energy	ΔE	5.064e5	3.513e5	J mol^{-1}	[66, 70]
Frequency factor	A	2.984e80	3.18e55	s^{-1}	[66, 70]

Table II

Complex tissue models for dynamic changes of acoustic attenuation/absorption coefficients and blood perfusion rate during thermal ablation.

Model No.	Relative blood perfusion, ω_{rel}	Relative acoustic absorption, α_{rel}
1	$\dot{m}_{rel}=\begin{cases} 1+30\cdot DS, 0<DS\le 0.02 \\ 1.86-13\cdot DS, 0.02<DS\le 0.08 \\ 0.884-0.79\cdot DS, 0.08<DS\le 0.97 \\ 3.87-3.87\cdot DS, 0.97<DS\le 1 \\ 0, \quad DS>1 \end{cases}$	$\alpha_{rel}=\begin{cases} 1, \log_{10}t_{43}\le 1.8 \\ 0.185\cdot(\log_{10}t_{43})+0.667, 1.8<\log_{10}t_{43}\le 7.2 \\ 2, \log_{10}t_{43}>7.2 \end{cases}$
2	$\dot{m}_{rel}=\begin{cases} 1+0.275\cdot t_{43}, t_{43}\le 2 \text{ min} \\ 1.733-0.0917\cdot t_{43}, 2<t_{43}\le 8 \text{ min} \\ 1.0274-0.0034\cdot t_{43}, 8<t_{43}\le 300 \text{ min} \\ 0, t_{43}>300 \text{ min} \end{cases}$	$\alpha_{rel}=\begin{cases} 1, \log_{10}t_{43}\le 1.8 \\ 0.185\cdot(\log_{10}t_{43})+0.667, 1.8<\log_{10}t_{43}\le 7.2 \\ 2, \log_{10}t_{43}>7.2 \end{cases}$
3	$\dot{m}_{rel}=\begin{cases} 1, \quad t_{43}\le 300 \text{ min} \\ 0, \quad t_{43}>300 \text{ min} \end{cases}$	$\alpha_{rel}=\begin{cases} 1, \log_{10}t_{43}\le 1.8 \\ 0.185\cdot(\log_{10}t_{43})+0.667, 1.8<\log_{10}t_{43}\le 7.2 \\ 2, \log_{10}t_{43}>7.2 \end{cases}$
4	$\dot{m}_{rel}=\begin{cases} 1, T\le 37\,^{\circ}C \\ 0.12-T\cdot 3.44, 37<T\le 42\,^{\circ}C \\ 7.9-0.15\cdot T, 42<T\le 46\,^{\circ}C \\ 4.29-0.07\cdot T, 46<T\le 60\,^{\circ}C \\ 0, T>60^{\circ}\,C \end{cases}$	$\alpha_{rel}=\begin{cases} 1, T\le 50\,^{\circ}C \\ 0.067\cdot t_{43}-2.333, 50<T\le 65\,^{\circ}C \\ 2, T>65\,^{\circ}C \end{cases}$
5	$\dot{m}_{rel}=\begin{cases} 1, \quad T\le 60\,^{\circ}C \\ 0, \quad T>60\,^{\circ}C \end{cases}$	$\alpha_{rel}=1$

Table III

Volume (cm^3) of the ablation zone as indicated by thermal dose ($t_{43} \geq 240$ min) and thermal damage measures ($\Omega \geq 4.6$) after 5, 10 and 15 min ablation with interstitial and transurethral applicators in prostate and liver tissue, computed using tissue models 1—5. Values listed in the table are for a nominal perfusion rate (2.5 kg m^{-3} s^{-1} for prostate and 15 kg m^{-3} s^{-1} for liver), while values in parentheses are for lower and higher perfusion rates, as listed in the text.

Ablation duration	Tissue Model	Necrosis Model	Interstitial 360° (Prostate)	Interstitial 180° (Prostate)	Interstitial 90° (Prostate)	Interstitial 360° (Liver)	Transurethral 90° (Prostate)
5 min	1	$t_{43} \geq 240$ min	10.8 (9.0—12.1)	5.8 (4.8—6.5)	4.0 (3.3—4.5)	7.3 (6.6—8.1)	7.2 (6.3—7.9)
		$\Omega \geq 4.6$	11.2 (9.3—12.7)	6.1 (5.1—7.0)	4.3 (3.6—4.8)	7.2 (6.5—8.1)	7.6 (6.6—8.4)
	2	$t_{43} \geq 240$ min	10.6 (8.7—12.0)	5.6 (4.7—6.5)	3.9 (3.2—4.4)	6.9 (6.2—7.8)	7.1 (6.1—7.8)
		$\Omega \geq 4.6$	11.0 (9.1—12.6)	6.0 (5.0—6.9)	4.2 (3.5—4.8)	6.8 (6.2—7.7)	7.5 (6.5—8.4)
	3	$t_{43} \geq 240$ min	10.6 (8.8—12.1)	5.6 (4.7—6.5)	3.9 (3.2—4.4)	7.0 (6.3—7.8)	7.1 (6.1—7.8)
		$\Omega \geq 4.6$	11.0 (9.1—12.6)	6.1 (5.0—6.9)	4.2 (3.5—4.8)	6.9 (6.2—7.7)	7.5 (6.5—8.4)
	4	$t_{43} \geq 240$ min	10.1 (8.2—11.7)	5.3 (4.3—6.2)	3.7 (3.0—4.3)	6.4 (5.8—7.2)	6.8 (5.8—7.6)
		$\Omega \geq 4.6$	10.6 (8.5—12.2)	5.7 (4.6—6.7)	4.0 (3.3—4.6)	6.4 (5.7—7.2)	7.2 (6.1—8.1)
	5	$t_{43} \geq 240$ min	13.1 (10.2—15.8)	7.3 (5.2—9.0)	6.1 (4.8—7.3)	3.9 (2.7—5.4)	9.1 (7.3—10.5)
		$\Omega \geq 4.6$	13.9 (10.9—16.4)	7.8 (5.7—9.5)	6.6 (5.2—7.8)	3.9 (2.7—5.4)	9.7 (7.9---11.1)
10 min	1	$t_{43} \geq 240$ min	19.7 (15.6—23.6)	9.8 (7.6—11.9)	6.5 (5.1—7.8)	10.5 (9.4—11.9)	10.4 (8.6—12.1)
		$\Omega \geq 4.6$	21.9 (17.2—26.6)	11.4 (8.8—14.1)	7.7 (6.0—5.3)	10.6 (9.5—11.9)	12.0 (9.8—14.1)
	2	$t_{43} \geq 240$ min	19.3 (15.1—23.3)	9.5 (7.4—11.7)	6.3 (4.9—7.7)	10.0 (9.0—11.4)	10.2 (8.4—12.0)
		$\Omega \geq 4.6$	21.5 (16.7—26.4)	11.2 (8.5—13.9)	7.5 (5.8—9.3)	10.1 (9.0—11.4)	11.8 (9.6—14.0)
	3	$t_{43} \geq 240$ min	19.2 (14.9—23.3)	9.5 (7.3—11.7)	6.3 (4.9—7.7)	9.9 (8.8—11.2)	10.2 (8.3—12.0)
		$\Omega \geq 4.6$	21.6 (16.7—26.4)	11.2 (8.5—14.0)	7.5 (5.8—9.3)	9.9 (8.9—11.3)	11.8 (9.5—14.0)
	4	$t_{43} \geq 240$ min	17.7 (13.3—22.3)	8.6 (6.3—11.1)	5.7 (4.3—7.3)	8.2 (7.3—9.5)	9.4 (7.5—11.5)
		$\Omega \geq 4.6$	19.9 (14.9—25.1)	10.2 (7.4—13.2)	6.9 (5.1—8.8)	8.3 (7.4—9.6)	10.9 (8.6—13.4)
	5	$t_{43} \geq 240$ min	24.9 (17.6—32.7)	13.4 (8.5—18.5)	10.0 (7.1—13.1)	5.5 (3.4—8.1)	13.6 (10.1—17.4)
		$\Omega \geq 4.6$	28.5 (20.4—37.0)	15.9 (10.4—21.6)	12.0 (8.6—15.2)	5.7 (3.6—8.3)	16.0 (12.0—20.2)
15 min	1	$t_{43} \geq 240$ min	26.2 (19.1—32.9)	12.5 (9.3—16.1)	8.2 (6.2—10.4)	12.1 (10.9—13.9)	12.5 (10.0—15.2)
		$\Omega \geq 4.6$	30.6 (22.8—39.2)	15. 7 (11.4—20.6)	10.3 (7.7—13.4)	12.3 (11.0—14.1)	15.2 (11.9—18.9)
	2	$t_{43} \geq 240$ min	25.5 (19.2—32.5)	12.2 (9.0—15.9)	8.0 (6.0—10.2)	11.6 (10.4—13.3)	12.3 (9.7—15.0)
		$\Omega \geq 4.6$	30.0 (22.1—38.7)	15.4 (11.1—20.3)	10.1 (7.5—13.3)	11.7 (10.5—13.5)	15.0 (11.7—18.7)
	3	$t_{43} \geq 240$ min	25.2 (18.8—32.3)	12.0 (8.8—15.8)	7.9 (5.9—10.2)	11.3 (10.0—12.9)	12.1 (9.6—14.9)
		$\Omega \geq 4.6$	29.9 (22.0—38.8)	15.3 (11.0—20.4)	10.1 (7.4—13.3)	11.4 (10.2—13.1)	14.9 (11.6—18.7)
	4	$t_{43} \geq 240$ min	22.4 (15.9—30.2)	10.5 (7.3—14.5)	6.9 (4.9—9.4)	8.8 (7.8—10.3)	10.9 (8.3—14.0)
		$\Omega \geq 4.6$	26.7 (18.8—36.3)	13.4 (9.2—18.8)	8.9 (6.2—12.3)	9.0 (7.9—10.5)	13.4 (10.0—17.5)
	5	$t_{43} \geq 240$ min	32.1 (21.4—45.5)	17.6 (10.4—25.4	12.2 (8.2—16.6)	6.6 (3.9—9.6)	16.2 (11.4—22.1)
		$\Omega \geq 4.6$	39.4 (26.5—55.0)	22.5 (13.6—31.7)	15.5 (10.7—20.3)	6.8 (4.2—10.0)	20.4 (14.4—27.2)